1 **Improved aerosol correction for OMI tropospheric NO$_2$ retrieval over East Asia:**

2 **constraint from CALIOP aerosol vertical profile**

3 Mengyao Liu[1,2], Jintai Lin[1], K. Folkert Boersma[2,3], Gaia Pinardi[4], Yang Wang[5], Julien

4 Chimot[6], Thomas Wagner[5], Pinghua Xie[7,8,9], Henk Eskes[2], Michel Van Roozendael[4],

5 François Hendrick[4], Pucai Wang[10], Ting Wang[10], Yingying Yan[1], Lulu Chen[1], Ruijing

6 Ni[1]

7 1, Laboratory for Climate and Ocean-Atmosphere Studies, Department of

8 Atmospheric and Oceanic Sciences, School of Physics, Peking University, Beijing,

9 China

10 2, Royal Netherlands Meteorological Institute, De Bilt, the Netherlands

11 3, Meteorology and Air Quality department, Wageningen University, Wageningen,

12 the Netherlands

13 4, Royal Belgian Institute for Space Aeronomy (BIRA-IASB), Brussels, Belgium

14 5, Max Planck Institute for Chemistry, Mainz, Germany

15 6, Department of Geoscience and Remote Sensing (GRS), Civil Engineering and

16 Geosciences, TU Delft, the Netherlands

17 7, Anhui Institute of Optics and Fine Mechanics, Key laboratory of Environmental

18 Optics and Technology, Chinese Academy of Sciences, Hefei, China

19 8, CAS Center for Excellence in Urban Atmospheric Environment, Institute of Urban

20 Environment, Chinese Academy of Sciences, Xiamen, China

21 9, School of Environmental Science and Optoelectronic Technology, University of

22 Science and Technology of China, Hefei, China

23 10, IAP/CAS, Institute of Atmospheric Physics, Chinese Academy of Sciences,

24 Beijing, China

25 Correspondence to: Jintai Lin (linjt@pku.edu.cn); K. Folkert Boersma

26 (folkert.boersma@knmi.nl)

27 **Abstract**

28 Satellite retrieval of vertical column densities (VCDs) of tropospheric nitrogen dioxide

29 (NO_2) is critical for NO_x pollution and impact evaluation. For regions with high aerosol

30 loadings, the retrieval accuracy is greatly affected by whether aerosol optical effects are

31 treated implicitly (as additional "effective" clouds) or explicitly, among other factors.

32 Our previous POMINO algorithm explicitly accounts for aerosol effects to improve the

33 retrieval especially in polluted situations over China, by using aerosol information from

34 GEOS-Chem simulations with further monthly constraints by MODIS/Aqua aerosol

35 optical depth (AOD) data. Here we present a major algorithm update, POMINO v1.1,

36 by constructing a monthly climatological data set of aerosol extinction profiles, based

37 on Level-2 CALIOP/CALIPSO data over 2007–2015, to better constrain the modeled

38 aerosol vertical profiles.

39 We find that GEOS-Chem captures the month-to-month variation of CALIOP aerosol

40 layer height but with a systematic underestimate by about 300–600 m (season and

41 location dependent), due to a too strong negative vertical gradient of extinction above

42 1 km. Correcting the model aerosol extinction profiles results in small changes in

43 retrieved cloud fraction, increases in cloud top pressure (within 2–6% in most cases),

44 and increases in tropospheric NO_2 VCD by 4–16% over China on a monthly basis in

45 2012. The improved NO_2 VCDs (in POMINO v1.1) are more consistent with

46 independent ground-based MAX-DOAS observations ($R^2 = 0.80$, NMB = -3.4%, for

47 162 pixels in 49 days) than POMINO ($R^2 = 0.80$, NMB = -9.6%), DOMINO v2 ($R^2 =$

48 0.68, NMB = -2.1%), and QA4ECV (R^2 = 0.75, NMB = -22.0%) are. Especially on

49 haze days, R^2 reaches 0.76 for POMINO v1.1, much higher than that for POMINO

50 (0.68), DOMINO v2 (0.38), and QA4ECV (0.34). Furthermore, the increase in cloud

51 pressure likely reveals a more realistic vertical relationship between cloud and aerosol

52 layers, with aerosols situated above the clouds in certain months instead of always

53 below the clouds. The POMINO v1.1 algorithm is a core step towards our next public

54 release of data product (POMINO v2), and it will also be applied to the recently

55 launched S5P-TropOMI sensor.

1. Introduction

57 Air pollution is a major environmental problem in China. In particular, China has

58 become the world's largest emitting country of nitrogen oxides (NO_X=NO+NO_2) due

59 to its rapid economic growth, heavy industries, coal-dominated energy sources, and

60 relatively weak emission control (Cui et al., 2016; Lin et al., 2014a; Stavrakou et al.,

61 2016; Zhang et al., 2009). Tropospheric vertical column densities (VCDs) of nitrogen

62 dioxide (NO_2) retrieved from the Ozone Monitoring Instrument (OMI) onboard the

63 Earth Observing System (EOS) Aura satellite have been widely used to monitor and

64 analyze NO_X pollution over China because of its high spatiotemporal coverage (e.g.

65 (Lin et al., 2010; Miyazaki and Eskes, 2013; Verstraeten et al., 2015; Zhao and Wang,

66 2009). However, NO_2 retrieved from OMI and other space-borne instruments are

67 subject to errors in the conversion process from radiance to VCD, particularly with

68 respect to the calculation of tropospheric air mass factor (AMF) that is used to convert

69 tropospheric slant column density to VCD (e.g. Boersma et al., 2011; Bucsela et al.,

70 2013; Lin et al., 2015; Lorente et al., 2017).

71 Most current-generation NO_2 algorithms do not explicitly account for the effects of

72 aerosols on NO_2 AMFs and on prerequisite cloud parameter retrievals. These retrievals

73 often adopt an implicit approach wherein cloud algorithms retrieve "effective cloud"

74   parameters that include the optical effects of aerosols. This implicit method is based on

75   aerosols exerting an effect on the top-of-atmosphere radiance level, whereas the

76   assumed cloud model does not account for the presence of aerosols in the atmosphere

77   (Stammes et al., 2008; Veefkind et al., 2016; Wang et al., 2008b; Wang and Stammes,

78   2014). In the absence of clouds, an aerosol optical thickness of 1 is then interpreted as

79   an effective cloud fraction of ± 0.10, and the value also depends on the aerosol

80   properties (scattering or absorbing), true surface albedo and geometry angles (Chimot

81   et al., 2016) with an effective cloud pressure closely related to the aerosol layer, at least

82   for aerosols of predominantly scattering nature (e.g. Boersma et al., 2004, 2011,

83   Castellanos et al., 2014, 2015). However, in polluted situations with high aerosol

84   loadings and more absorbing aerosol types, which often occur over China and many

85   other developing regions, the implicit method can result in considerable biases

86   (Castellanos et al., 2014, 2015; Chimot et al., 2016; Kanaya et al., 2014; Lin et al.,

87   2014b).

88   Lin et al. (2014b, 2015) established the POMINO NO_2 algorithm, which builds on the

89   DOMINO v2 algorithm (for OMI NO_2 slant columns and stratospheric correction), but

90   improves upon it through a more sophisticated AMF calculation over China. In

91   POMINO, the effects of aerosols on cloud retrievals and NO_2 AMFs are explicitly

92   accounted for. In particular, daily information on aerosol optical properties such as

93   aerosol optical depth (AOD), single scattering albedo (SSA), phase function and

94   vertical extinction profiles are taken from nested Asian GEOS-Chem v9-02 simulations.

95   The modeled AOD at 550 nm is further constrained by MODIS/Aqua monthly AOD,

96   with the correction applied to other wavelengths based on modeled aerosol refractive

97   indices (Lin et al., 2014b). However, the POMINO algorithm does not include an

98   observation-based constraint on the vertical profile of aerosols, whose altitude relative

99   to NO_2 has strong and complex influences on NO_2 retrieval (Castellanos et al., 2015;

100   Leitão et al., 2010; Lin et al., 2014b). This study improves upon the POMINO algorithm

101   by incorporating CALIOP monthly climatology of aerosol vertical extinction profiles

102   to correct for model biases.

103   The CALIOP lidar, carried on the sun-synchronous CALIPSO satellite, has been

104   acquiring global aerosol extinction profiles since June 2006 (Winker et al., 2010).

105   CALIPSO and Aura are both parts of the National Aeronautics and Space

106   Administration (NASA) A-train constellation of satellites. The overpass time of

107   CALIOP/CALIPSO is only 15 minutes later than OMI/Aura. In spite of issues with the

108   detection limit, radar ratio selection and cloud contamination that cause some biases in

109   CALIOP aerosol extinction vertical profiles (Amiridis et al., 2015; Koffi et al., 2012;

110   Winker et al., 2013), comparisons of aerosol extinction profiles between ground-based

111   lidar and CALIOP show good agreements (Kacenelenbogen et al., 2014; Kim et al.,

112   2009; Misra et al., 2012). However, CALIOP is a nadir-viewing instrument that

113   measures the atmosphere along the satellite ground-track with a narrow field-of-view.

114   This means that the daily geographical coverage of CALIOP is much smaller than that

115   of OMI. Thus previous studies often used monthly/seasonal regional mean CALIOP

116   data to study aerosol vertical distributions or to evaluate model simulations (Chazette

117   et al., 2010; Johnson et al., 2012; Koffi et al., 2012; Ma and Yu, 2014; Sareen et al.,

118   2010).

119   There exist a few CALIOP Level-3 gridded datasets, such as LIVAS (Amiridis et al.

120   2015) and NASA official Level-3 monthly dataset (Winker et al., 2013). However,

121   LIVAS is an annual average day-night combined product, not suitable to be applied to

122   OMI NO_2 retrievals (around early afternoon, and in need of a higher temporal resolution

123   than annual). The horizontal resolution (2^0 long. $\times$ 5^0 lat.) of NASA official product

124   is much coarser than OMI footprints and the GEOS-Chem model resolution.

125   Here we construct a custom monthly climatology of aerosol vertical extinction profiles

126   based on 9-years (2007–2015) worth of CALIOP Version 3 Level-2 532 nm data. On a

127 climatological basis, we use the CALIOP monthly data to adjust GEOS-Chem profiles

128 in each grid cell for each day of the same month in any year. We then use the corrected

129 GEOS-Chem vertical extinction profiles in the retrievals of cloud parameters and NO_2.

130 Finally, we evaluate our updated POMINO retrieval (hereafter referred to as POMINO

131 v1.1), our previous POMINO product, DOMINO v2, and the newly released Quality

132 Assurance for Essential Climate Variables product (QA4ECV, see Appendix A), using

133 ground-based MAX-DOAS NO_2 column measurements at three urban/suburban sites

134 in East China for the year of 2012 and several months in 2008/2009.

135 Section 2 describes the construction of CALIOP aerosol extinction vertical profile

136 monthly climatology, the POMINO v1.1 retrieval approach, and the MAX-DOAS data.

137 It also presents the criteria for comparing different NO_2 retrieval products and for

138 selecting coincident OMI and MAX-DOAS data. Section 3 compares our CALIOP

139 climatology with NASA's official Level-3 CALIOP dataset and GEOS-Chem

140 simulation results. Sections 4 and 5 compare POMINO v1.1 to POMINO to analyze the

141 influence of improved aerosol vertical profiles on retrievals of cloud parameters and

142 NO_2 VCDs, respectively. Section 6 evaluates POMINO, POMINO v1.1, DOMNO v2,

143 and QA4ECV NO_2 VCD products using the MAX-DOAS data. Section 7 concludes

144 our study.

145 **2. Data and methods**

146 2.1 CALIOP monthly mean extinction profile climatology

147 CALIOP is a dual-wavelength polarization lidar measuring attenuated backscatter

148 radiation at 532 and 1064 nm since June 2006. The vertical resolution of aerosol

149 extinction profiles is 30 m below 8.2 km and 60 m up to 20.2 km (Winker et al., 2013),

150 with a total of 399 sampled altitudes. The horizontal resolution of CALIOP scenes is

151 335 m along the orbital track and is given over a 5 km horizontal resolution in Level-2

152 data.

153 As detailed in Appendix B, we use the daily all-sky Version 3 CALIOP Level-2 aerosol

154 profile product at 532 nm from 2007 to 2015 to construct a monthly Level-3

155 climatological dataset of aerosol extinction profiles over China and nearby regions.

156 This dataset is constructed on the GEOS-Chem model grid (0.667^o long. x 0.5^o lat.)

157 and vertical resolution (47 layers, with 36 layers or so in the troposphere). The ratio of

158 climatological monthly CALIOP to monthly GEOS-Chem profiles represents the

159 scaling profile to adjust the daily GEOS-Chem profiles in the same month (see Sect.

160 2.2)

161 *2.2 POMINO v1.1 retrieval approach*

162 The NO_2 retrieval consists of three steps. First, the total NO_2 slant columns density

163 (SCD) is retrieved using the Differential Optical Absorption Spectroscopy (DOAS)

164 technique (for the 405-465 nm spectral window in the case of OMI). The uncertainty

165 of the SCD is determined by the appropriateness of the fitting technique, the instrument

166 noise, the choice of fitting window, and the orthogonality of the absorbers' cross

167 sections (Bucsela et al., 2006; van Geffen et al., 2015; Lerot et al., 2010; Richter et al.,

168 2011; Zara et al., 2018). The NO_2 SCD in DOMINO v2 has a bias at about 0.5~1.3 $\times$

169 10^{15} molec. cm^{-2} (Belmonte Rivas et al., 2014; Dirksen et al., 2011; van Geffen et al.,

170 2015; Marchenko et al., 2015; Zara et al., 2018), which can be reduced by improving

171 wavelength calibration and including O_2-O_2 and liquid water absorption in the fitting

172 model (van Geffen et al., 2015; Zara et al., 2018). The tropospheric SCD is then

173 obtained by subtracting the stratospheric SCD from the total SCD. The bias in the total

174 SCD is mostly absorbed by this stratospheric separation step, which may not propagate

175 into the tropospheric SCD (van Geffen et al., 2015). The last step converts the

176 tropospheric SCD to VCD by using the tropospheric AMF (VCD = SCD / AMF). The

177 tropospheric AMF is calculated at 438 nm by using look-up tables (in most retrieval

178 algorithms) or online radiative transfer modeling (in POMINO) driven by ancillary

179 parameters, which act as the dominant source of errors in retrieved NO_2 VCD data over

180 polluted areas (Boersma et al., 2007; Lin et al., 2014b, 2015; Lorente et al., 2017).

181 Our POMINO algorithm focuses on the tropospheric AMF calculation over China and

182 nearby regions, taking the tropospheric SCD (Dirksen et al., 2011) from DOMINO v2

183 (Boersma et al., 2011). POMINO improves upon the DOMINO v2 algorithm in the

184 treatment of aerosols, surface reflectance, online radiative transfer calculations, spatial

185 resolution of NO_2, temperature and pressure vertical profiles, and consistency between

186 cloud and NO_2 retrievals (Lin et al., 2014b, 2015). In brief, we use the parallelized

187 LIDORT-driven AMFv6 package to derive both cloud parameters and tropospheric

188 NO_2 AMFs for individual OMI pixels online (rather than using a look-up table). NO_2

189 vertical profiles, aerosol optical properties and aerosol vertical profiles are taken from

190 the nested GEOS-Chem model over Asia (0.667^{0} long.$\times$ 0.5^{0} lat. before May 2013

191 and 0.3125^{0} long.$\times$ 0.25^{0} lat. afterwards), and pressure and temperature profiles are

192 taken from the GEOS-5 and GEOS-FP assimilated meteorological fields that drive

193 GEOS-Chem simulations. Model aerosols are further adjusted by satellite data (see

194 below). We adjust the pressure profiles based on the difference in elevation between

195 the pixel center and the matching model grid cell (Zhou et al., 2010). We also account

196 for the effects of surface bidirectional reflectance distribution function (BRDF) (Lin et

197 al., 2014b; Zhou et al., 2010) by taking three kernel parameters (isotropic, volumetric

198 and geometric) from the MODIS MCD43C2 data set at 440 nm (Lucht et al., 2000).

199 As a prerequisite to the POMINO NO_2 retrieval, clouds are retrieved through the O_2-

200 O_2 algorithm (Acarreta et al., 2004; Stammes et al., 2008) with O_2-O_2 SCDs from

201 OMCLDO2, and with pressure, temperature, surface reflectance, aerosols and other

202 ancillary information consistent with the NO_2 retrieval. Note that the treatment of cloud

203   scattering (as "effective" Lambertian reflector, as in other NO_2 algorithms) is different

204   from the treatment of aerosol scattering/absorption (vertically resolved based on the

205   Mie scheme).

206   POMINO uses the temporally and spatially varying aerosol information, including

207   AOD, single scattering albedo (SSA), phase function and vertical profiles from GEOS-

208   Chem simulations. POMINO v1.1 (this work) further uses CALIOP data to constrain

209   the shape of aerosol vertical extinction profile. We run the model at a resolution of

210   0.3125^o long.$\times 0.25^o$ lat. before May 2013 and 0.667^o long.$\times 0.5^o$ lat. afterwards, as

211   determined by the resolution of the driving meteorological fields. We then regrid the

212   finer resolution model results to 0.667^o long.$\times 0.5^o$ lat., to be consistent with the

213   CALIOP data grid. We then sample the model data at times and locations with valid

214   CALIOP data at 532 nm to establish the model monthly climatology.

215   For any month in a grid cell, we divide the CALIOP monthly climatology of aerosol

216   extinction profile shape by model climatological profile shape to obtain a unitless

217   scaling profile (Eq. 1), and apply this scaling profile to all days of that month in all

218   years (Eq. 2). Such a climatological adjustment is based on the assumption that

219   systematic model limitations are month-dependent and persist over the years and days

220   (e.g., a too strong vertical gradient, see Sect. 3.3). Although this monthly adjustment

221   means discontinuity on the day-to-day basis (e.g., from the last day of a month to the

222   first day of the next month), such discontinuity does not significantly affect the NO_2

223   retrieval, based on our sensitivity test.

224   In Eqs. 1 and 2, E^C represents the CALIOP climatological aerosol extinction

225   coefficient, E^G the GEOS-Chem extinction, E^{Gr} the post-scaling model extinction,

226   and R the scaling profile. The subscript i denotes a grid cell, k a vertical layer, d a day,

227   m a month, and y a year. Note that in Eq. 1, the extinction coefficient at each layer is

228   normalized relative to the maximum value of that profile. This procedure ensures that

229 the scaling is based on the relative shape of the extinction profile and is thus

230 independent of the accuracies of CALIOP and GEOS-Chem AOD. We keep the

231 absolute AOD value of GEOS-Chem unchanged in this step.

232 $\quad R_{i,k,m} = \dfrac{E_{i,k,m}^{C}/\max\,(E_{i,k,m}^{C})}{E_{i,k,m}^{G}/max\,(E_{i,k,m}^{G})}$ (1)

233 $\quad E_{i,k,d,m,y}^{Gr} = E_{i,k,d,m,y}^{G} \times R_{i,k,m}$ (2)

234 In POMINO, the GEOS-Chem AOD are further constrained by a MODIS/Aqua

235 Collection 5.1 monthly AOD dataset compiled on the model grid (Lin et al., 2014b,

236 2015). POMINO v1.1 uses the Collection 5.1 AOD data before May 2013 and

237 Collection 6 data afterwards. For adjustment, model AOD are projected to a

238 0.667^{0} long.$\times$ 0.5^{0} lat. grid and then sampled at times and locations with valid MODIS

239 data (Lin et al., 2015). As shown in Eq. 3, τ^{M} denotes MODIS AOD, τ^{G} GEOS-

240 Chem AOD, and τ^{Mr} post-adjustment model AOD. The subscript i denotes a grid

241 cell, d a day, m a month, and y a year. This AOD adjustment ensures that in any month,

242 monthly mean GEOS-Chem AOD is the same as MODIS AOD while the modeled day-

243 to-day variability is kept.

244 $\quad \tau_{i,d,m,y}^{Gr} = \dfrac{\tau_{i,m,y}^{M}}{\tau_{i,m,y}^{G}} \times \tau_{i,d,m,y}^{G}$ (3)

245 Equations 4–5 show the complex effects of aerosols in calculating the AMF for any

246 pixel. The AMF is the linear sum of tropospheric layer contributions to the slant column

247 weighted by the vertical sub columns (Eq. 4). The box AMF, amf_{k}, describes the

248 sensitivity of NO$_2$ SCD to layer k, and $x_{a,k}$ represent the subcolumn of layer k from

249 a priori NO$_2$ profile. The l represent the first integrated layer, which is the layer above

250 the ground for clear sky, or the layer above cloud top for cloudy sky. The t represent

251 the tropopause layer. POMINO assumes the independent pixel approximation (IPA)

252 (Martin et al., 2002; Boersma et al., 2002). This means that the calculated AMF for any

253 pixel consists of a fully cloudy-sky portion (AMF_{clr}) and a fully clear-sky portion

254 (AMF_{cld}), with weights based on the cloud radiance fraction ($CRF = \frac{CF \cdot I_{cld}}{(1-CF) \cdot I_{clr} + CF \cdot I_{cld}}$,

255 where I_{clr} and I_{cld} are radiance from the clear-sky part and fully cloudy part of the

256 pixel, respectively.) (Eq. 5). AMF_{cld} is affected by above-cloud aerosols, and AMF_{clr}

257 is affected by aerosols in the entire column. Also, aerosols affect the retrieval of CRF.

258 Thus, the improvement of aerosol vertical profile in POMINO v1.1 affects all the three

259 quantities in Eq. 5 and thus leads to complex impacts on retrieved NO_2 VCD.

260 $AMF = \frac{\sum_l^t amf_k x_{a,k}}{\sum_l^t x_{a,k}}$ (4)

261 $AMF = AMF_{cld} \cdot CRF + AMF_{clr} \cdot (1 - CRF)$ (5)

262 2.3 OMI pixel selection to evaluate POMINO v1.1, POMINO, DOMINO v2, and

263 QA4ECV

264 We exclude OMI pixels affected by row anomaly (Schenkeveld et al., 2017) or with

265 high albedo caused by icy/snowy ground. To screen out cloudy scenes, we choose

266 pixels with CRF below 50% (effective cloud fraction is typically below 20%) in

267 POMINO.

268 The selection of CRF threshold influences the validity of pixels. The "effective" CRF

269 in DOMINO implicitly includes the influence of aerosols. In POMINO, the aerosol

270 contribution is separated from that of the clouds, resulting in a lower CRF than for

271 DOMINO. The CRF differs insignificantly between POMINO and POMINO v1.1,

272 because the same AOD and other non-aerosol ancillary parameters are used in the

273 retrieval process. Using the CRF from POMINO instead of DOMINO or QA4ECV for

274 cloud screening means that the number of "valid" pixels in DOMINO increases by

275 about 25%, particularly because much more pixels with high pollutant (aerosol and NO_2)

276   loadings are now included. This potentially reduces the sampling bias (Lin et al., 2014b,

277   2015), and the ensemble of pixels now includes scenes with high "aerosol radiative

278   fractions". Further research is needed to fully understand how much these high-aerosol

279   scenes may be subject to the same screening issues as the cloudy scenes. Nevertheless,

280   the limited evidence here and in Lin et al. (2014b, 2015) suggests that including these

281   high-aerosol scenes does not affect the accuracy of NO_2 retrieval.

282   2.4 MAX-DOAS data

283   We use MAX-DOAS measurements at three suburban or urban sites in East China,

284   including one urban site at the Institute of Atmospheric Physics (IAP) in Beijing

285   (116.38° E, 39.38 ° N), one suburban site in Xianghe County (116.96° E, 39.75 ° N)

286   to the south of Beijing, and one urban site in the Wuxi City (120.31° E, 31.57 ° N) in

287   the Yangzi River delta (YRD). Figure 1 shows the locations of these sites overlaid with

288   POMINO v1.1 NO_2 VCDs in August 2012. Table 1 summarizes the information of

289   MAX-DOAS measurements.

290   The instruments in IAP and in Xianghe were designed at BIRA-IASB (Clémer et al.,

291   2010). Such an instrument is a dual-channel system composed of two thermally

292   regulated grating spectrometers, covering the ultraviolet (300–390 nm) and visible

293   (400–720 nm) wavelengths. It measures scattered sunlight every 15 minutes at nine

294   elevation angles: 2°, 4°, 6°, 8°, 10°, 12°, 15°, 30°, and 90°. The telescope

295   of the instrument is pointed to the north. The data are analyzed following Hendrick et

296   al. (2014). The Xianghe suburban site is influenced by pollution from the surrounding

297   major cities like Beijing and Tianjin. At Xianghe, MAX-DOAS data are data are

298   continuously available since early 2011, and data in 2012 are used here for comparison

299   with OMI products. At IAP, MAX-DOAS data are available in 2008 and 2009 (Table

300   1), thus for comparison purposes we process OMI products to match the MAX-DOAS

301   times.

302   Located on the roof of an 11-story building, the instrument at Wuxi was developed by

303   Anhui Institute of Optics and Fine Mechanics (AIOFM) (Wang et al., 2015, 2017a). Its

304   telescope is pointed to the north and records at five elevation angles (5°, 10^0, 20^0, 30^0,

305   and 90^0). Wuxi is a typical urban site affected by heavy NO_x and aerosol pollution. The

306   measurements used here are analyzed in Wang et al. (2017a). Data are available in 2012

307   for comparison with OMI products.

308   When comparing the four OMI products against MAX-DOAS observations, temporal

309   and spatial inconsistency in sampling is inevitable. The spatial inconsistency, together

310   with the substantial horizontal inhomogeneity in NO_2, might be more important than

311   the influence of temporal inconsistency (Wang et al., 2017b). The influence of the

312   horizontal inhomogeneity was suggested to be about 10–30% for MAX-DOAS

313   measurements in Beijing (Lin et al., 2014b; Ma et al., 2013) and 10–15% for less

314   polluted locations like Tai'an, Mangshan and Rudong (Irie et al., 2012). Following

315   previous studies, we average MAX-DOAS data within 1 h of the OMI overpass time,

316   and we select OMI pixels within 25 km of a MAX-DOAS site whose viewing zenith

317   angle is below 30°. To exclude local pollution events near the MAX-DOAS site (such

318   as the abrupt increase of NO_2 caused by the pass of consequent vehicles during a very

319   short period), the standard deviation of MAX-DOAS data within 1 h should not exceed

320   20% of their mean value (Lin et al., 2014b). We elect not to spatially average the OMI

321   pixels because they can reflect the spatial variability in NO_2 and aerosols.

322   We further exclude MAX-DOAS data in cloudy conditions, as clouds can cause large

323   uncertainties in MAX-DOAS and OMI data. To find the actual cloudy days, we use

324   MODIS/Aqua cloud fraction data, MODIS/Aqua Level-3 corrected reflectance (true

325   color) data at the $1° \times 1°$ resolution, and current weather data observed from the

326   nearest ground meteorological station (indicated by the black triangles in Fig. 1b).

327   Since there is only one meteorological station available near the Beijing area, it is used

328   for both IAP and Xianghe MAX-DOAS sites. We first use MODIS/Aqua corrected

329   reflectance (true color) to distinguish clouds from haze. For cloudy days determined by

330   the reflectance checking, we examine both the MODIS/Aqua cloud fraction data and

331   the meteorological station cloud records, considering that MODIS/Aqua cloud fraction

332   data may be missing or have a too coarse horizontal resolution to accurately interpret

333   the cloud conditions at the MAX-DOAS site. We exclude MAX-DOAS NO_2 data if the

334   MODIS/Aqua cloud fraction is larger than 60% and the meteorological station reports

335   a "BROKEN" (cloud fraction ranges from 5/8 to 7/8) or "OVERCAST" (full cloud

336   cover) sky. For the three MAX-DOAS sites together, this leads to 49 days with valid

337   data out of 64 days with pre-screening data.

338   We note here that using cloud fraction data from MODIS/Aqua or MAX-DOAS (for

339   Xianghe only, see Gielen et al., 2014) alone to screen cloudy scenes may not be

340   appropriate on heavy-haze days.   For example, on 8th January, 2012, MODIS/Aqua

341   cloud fraction is about 70–80% over the North China Plain and MAX-DOAS at

342   Xianghe suggests the presence of "thick clouds". However, both the meteorological

343   station and MODIS/Aqua corrected reflectance (true color) product suggest that the

344   North China Plain was covered by a thick layer of haze. Consequently, this day was

345   excluded from the analysis.

346   **3. Monthly climatology of aerosol extinction profiles from CALIOP and GEOS-**

347   **Chem**

348   3.1 CALIOP monthly climatology

349   The aerosol layer height (ALH) is a good indicator to what extent aerosols are mixed

350   vertically (Castellanos et al., 2015). As defined in Eq. A1 in Appendix B, the ALH is

351   the average height of aerosols weighted by vertically resolved aerosol extinction. Figure

352   2a shows the spatial distribution of our CALIOP ALH climatology in each season. At

353   most places, the ALH reaches a maximum in spring or summer and a minimum in fall

354   or winter. The lowest ALH in fall and winter can be attributed to heavy near-surface

355   pollution and weak vertical transport. The high values in summer are related to strong

356   convective activities. Over the north, the high values in spring are partly associated with

357   Asian dust events, due to high surface winds and dry soil in this season (Huang et al.,

358   2010; Proestakis et al., 2017; Wang et al., 2010), which also affects the oceanic regions

359   via atmospheric transport. The springtime high ALH over the south may be related to

360   the transport of carbonaceous aerosols from Southeast Asian biomass burning (Jethva

361   et al., 2016). Averaged over the domain, the seasonal mean ALHs are 1.48 km, 1.43

362   km, 1.27km, 1.18 km in spring, summer, fall and winter.

363   Figure 3a,b further shows the climatological monthly variations of ALH averaged over

364   Northern East China (the anthropogenic source region shown in orange in Fig. 1a) and

365   Northwest China (the dust source region shown in yellow in Fig. 1a). The two regions

366   exhibit distinctive temporal variations. Over Northern East China, the ALH reaches a

367   maximum in April (~1.53 km) and a minimum in December (~1.14 km). Over

368   Northwest China, the ALH peaks in August (~1.59km) because of strongest convection

369   (Zhu et al., 2013), although the springtime ALH is also high.

370   Figure 4a shows the climatological seasonal regional average vertical profiles of aerosol

371   extinction over Northern East China. Here, the aerosol extinction increases from the

372   ground level to a peak at about 300–600 m (season dependent), above which it

373   decreases gradually. The height of peak extinction is lowest in winter, consistent with

374   a stagnant atmosphere, thin mixing layer, and increased emissions (from residential and

375   industrial sectors). The large error bars (horizontal lines in different layers, standing for

376   1 standard deviation) indicate strong spatiotemporal variability of aerosol extinction.

377   Over Northwest China (Fig. 5a), the column total aerosol extinction is much smaller

378   than that over Northern East China (Fig. 4a), due to lower anthropogenic sources and

379   dominant natural dust emissions. Vertically, the decline of extinction from the peak-

380   extinction height to 2 km is also much more gradual than the decline over Northern East

381   China, indicating stronger lifting of surface emitted aerosols. In winter, the column total

382   aerosol extinction is close to the high value in dusty spring, whereas the vertical

383   gradient of extinction is strongest among the seasons. This reflects the high

384   anthropogenic emissions in parts of Northwest China, which have been rapidly

385   increasing in the 2000s due to relatively weak emission control supplemented by

386   growing activities of relocation of polluted industries from the eastern coastal regions

387   (Cui et al., 2016; Zhao et al., 2015).

388   Overall, the spatial and seasonal variations of CALIOP aerosol vertical profiles are

389   consistent with changes in meteorological conditions, anthropogenic sources, and

390   natural emissions. The data will be used to evaluate and adjust GEOS-Chem simulation

391   results in Sect. 3.2. A ccomparison of our CALIOP dataset with NASA's official Level-

392   3 data is presented in Appendix C.

393   3.2 Evaluation of GEOS-Chem aerosol extinction profiles

394   Figure 2b shows the spatial distribution of seasonal ALHs simulated by GEOS-Chem.

395   The model captures the spatial and seasonal variations of CALIOP ALH (Fig. 2a) to

396   some degree, with an underestimate by about 0.3 km on average.   The spatial

397   correlation between CALIOP (Fig. 2a) and GEOS-Chem (Fig. 2b) ALH is 0.37 in

398   spring, 0.57 in summer, 0.40 in fall, and 0.44 in winter. The spatiotemporal consistency

399   and underestimate is also clear from the regional mean monthly ALH data in Fig. 3 –

400   the temporal correlation between GEOS-Chem and CALIOP ALH is 0.90 in Northern

401   East China and 0.97 in Northwest China.

402   Figures 4a and 5a show the GEOS-Chem simulated 2007–2015 monthly climatological

403   vertical profiles of aerosol extinction coefficient over Northern East China and

404   Northwest China, respectively. Over Northern East China (Fig. 4a), the model (red line)

405   captures the vertical distribution of CALIOP extinction (black line) below the height of

406   1 km, despite a slight underestimate in the magnitude of extinction and an overestimate

407   in the peak-extinction height. From 1 to 5 km above the ground, the model substantially

408   overestimates the rate of decline in extinction coefficient with increasing altitude.

409   Across the seasons, GEOS-Chem underestimates the magnitude of aerosol extinction

410   by up to 37% (depending on the height). Over Northwest China (Fig. 5a), GEOS-Chem

411   has an underestimate in all seasons, with the largest bias by about 80% in winter likely

412   due to underestimated water-soluble aerosols and dust emissions (Li et al., 2016; Wang

413   et al., 2008a).

414   Since the POMINO v1.1 algorithm uses MODIS AOD to adjust model AOD, it only

415   uses the CALIOP aerosol extinction profile shape to adjust the modeled shape (Eqs. 1

416   and 2). Figures 4b and 4b show the vertical shapes of aerosol extinction, averaged

417   across all profiles in each season over Northern East China and Northwest China,

418   respectively. Over Northern East China (Fig. 4b), GEOS-Chem underestimates the

419   CALIOP values above 1 km by 52–71%. This underestimate leads to a lower ALH,

420   consistent with the finding by van Donkelaar et al. (2013) and Lin et al. (2014b). Over

421   Northwest China (Fig. 5b), the model also underestimates the CALIOP values above 1

422   km by 50–62%. These results imply the importance of correcting the modeled aerosol

423   vertical shape prior to cloud and NO_2 retrievals.

424   **4. Effects of aerosol vertical profile improvement on cloud retrieval in 2012**

425   Figure 6a, b shows the monthly average ALH and cloud top height (CTH,

426   corresponding to cloud pressure, CP) over Northern East China and Northwest China

427   in 2012. In order to discuss the CTH, only cloudy days are analyzed here, by excluding

428   days with zero cloud fraction (CF = 0, clear-sky cases) in POMINO. Although "clear

429   sky" is used sometimes in the literature to represent low cloud coverage (e.g., CF < 0.2

430   or CRF < 0.5, Boersma et al., 2011; Chimot et al., 2016), here it strictly means CF = 0

431   while "cloudy sky" means CF > 0. About 62.7% of days contain non-zero fractions of

432   clouds over Northern East China, and the number is 59.1% for Northwest China. The

433   CF changes from POMINO to POMINO v1.1 (i.e., after aerosol vertical profile

434   adjustment) are negligible (within $\pm$0.5%, not shown) due to the same values of AOD

435   and SSA used in both products. This is because overall CF is mostly driven by the

436   continuum reflectance at 475 nm (mainly determined by AOD and surface reflectance,

437   which remain unchanged), which is insensitive of aerosol profile but CTH is driven by

438   the O_2-O_2 SCD, which is itself impacted by ALH.

439   Figure 6a, b shows that over the two regions, the CTH varies notably from one month

440   to another, whereas the ALH is much more stable across the months. Over Northern

441   East China, the ALH increases by 0.52 km from POMINO (orange dashed line) to

442   POMINO v1.1 (orange solid line) due to the CALIOP-based monthly climatological

443   adjustment. The increase in ALH means a stronger "shielding" effect of aerosols on the

444   O_2-O_2 absorbing dimer, which, in turn, results in a reduced CTH by 0.69 km on average.

445   For POMINO over Northern East China (Fig. 6a), the retrieved clouds usually extend

446   above the aerosol layer, i.e., the CTH (grey dashed line) is much larger than the ALH

447   (orange dashed line). Using the CALIOP climatology in POMINO v1.1 results in the

448   ALH higher than the CTH in fall and winter. The more elevated ALH is consistent with

449   the finding of Jethva et al. (2016) that a significant amount of absorbing aerosols resides

450   above clouds over Northern East China based on 11-year (2004–2015) OMI near-UV

451   observations.

452   The CTH in Northwest China is much lower than in Northern East China (Fig. 6a versus

453   7b). This is because the dominant type of actual clouds is (optically thin) cirrus over

454   western China (Wang et al., 2014), which is interpreted by the O_2-O_2 cloud retrieval

455   algorithm as reduced CTH (with cloud base from the ground). The reduction in CTH

456   from POMINO to POMINO v1.1 over Northwest China is also smaller than the

457   reduction over Northern East China, albeit with a similar enhancement in ALH, due to

458   lower aerosol loadings (Fig. 6c versus 6d).

459   Figure 7g,h presents the relative change in CP from POMINO to POMINO v1.1 as a

460   function of AOD (binned at an interval of 0.1) and changes in ALH from POMINO to

461   POMINO v1.1 (ΔALH, binned every 0.2 km) across all pixels in 2012 over Northern

462   East China. Results are separated for low cloud fraction (CF < 0.05 in POMINO, Fig.

463   7g) and modest cloud fraction (0.2 < CF < 0.3, Fig. 7h). The median of the CP changes

464   for pixels within each AOD and ΔALH bin is shown. Figure 7e,f presents the

465   corresponding numbers of occurrence under the two cloud conditions.

466   Figure 7 shows that over Northern East China, the increase in ALH is typically within

467   0.6 km for the case of CF < 0.05 (Fig. 7e), and the corresponding increase in CP is

468   within 6% (Fig. 7g). In this case, the average CTH (2.95 km in POMINO versus 1.58

469   km in POMINO v1.1) becomes much lower than the average ALH (1.06 km in

470   POMINO versus 1.98 km in POMINO v1.1). For the case with CF between 0.2 and 0.3,

471   the increase in ALH is within 1.2 km for most scenes (Fig. 7f), which leads to a CP

472   change of 2% (Fig. 7h), much smaller than the CP change for CF < 0.05 (Fig. 7g). This

473   is partly because the larger the CF is, the smaller a change in CF is required to

474   compensate for the ΔALH in the O_2-O_2 cloud retrieval algorithm. Furthermore, with

475   0.2 < CF < 0.3, the mean value of CTH is much higher than ALH in both POMINO

476   (2.76 km for CTH versus 1.13km for ALH) and POMINO v1.1 (2.60km for CTH versus

477   2.09 km for ALH), thus a large portion of clouds are above aerosols so that the change

478   in CP is less sensitive to ΔALH. We find that the summertime data contribute the

479   highest portion (36.5%) to the occurrences for 0.2 < CF < 0.3.

480   For Northwest China (not shown), the dependence of CP changes to AOD and ΔALH

481   is similar to that for Northern East China. In particular, the CP change is within 10%

482   on average for the case of CF < 0.05 and 1.5% for the case of 0.2 < CF < 0.3.

483   **5. Effects of aerosol vertical profile improvement on NO$_2$ retrieval in 2012**

484   Figure 7a presents the percentage changes in clear-sky NO$_2$ VCD from POMINO to

485   POMINO v1.1 as a function of binned AOD and ΔALH over Northern East China. Here,

486   clear-sky pixels are chosen based on CF = 0 in POMINO. In any AOD bin, an increase

487   in ΔALH leads to an enhancement in NO$_2$. And for any ΔALH, the change in VCD is

488   greater (smaller) when AOD becomes larger (smaller), which indicates that the NO$_2$

489   retrieval is more sensitive to ALH in high aerosol loading cases. Clearly, the change in

490   NO$_2$ is not a linear function of AOD and ΔALH.

491   For cloudy scenes (Fig. 7b,c, cloud data are based on POMINO), the change in NO$_2$

492   VCD is less sensitive to AOD and ΔALH. This is because the existence of clouds limits

493   the optical effect of aerosols on tropospheric NO$_2$. Figure 6a presents the nitrogen layer

494   height (NLH, defined as the average height of model simulated NO$_2$ weighted by its

495   volume mixing ratio in each layer) in comparison to the ALH and CLH over Northern

496   East China. The figure shows that the POMINO v1.1 CTH is higher than the NLH in

497   all months and higher than the ALH in warm months, which means a "shielding" effect

498   on both NO$_2$ and aerosols.

499   Over Northwest China (not shown), the changes in clear-sky NO$_2$ VCD are within 9%

500   for most cases, which are much smaller than over Eastern China (within 18%). This is

501   because the NLH is much higher than the CLH and ALH (Fig. 6b) in absence of surface

502   anthropogenic emissions.

503   We convert the valid pixels into monthly mean Level-3 values datasets on a 0.25^0 long.

504   $\times$ 0.25^0 lat. grid. Figure 8a,b compares the seasonal spatial variations of NO_2 VCD in

505   POMINO v1.1 and POMINO in 2012. In both products, NO_2 peaks in winter due to the

506   longest lifetime and highest anthropogenic emissions (Lin, 2012). NO_2 also reaches a

507   maximum over Northern East China as a result of substantial anthropogenic sources.

508   From POMINO to POMINO v1.1, the NO_2 VCD increases by 3.4% (-67.5–41.7%) in

509   spring for the domain average (range), 3.0% (-59.5–34.4%) in summer, 4.6% (-15.3–

510   39.6%) in fall and 5.3% (-68.4–49.3%) in winter. The NO_2 change is highly dependent

511   on the location and season. The increase over Northern East China is largest in winter,

512   wherein the positive value for ΔALH implies that elevated aerosol layers "shield" the

513   NO_2 absorption.

514   **6. Evaluating satellite products using MAX-DOAS data**

515   We use MAX-DOAS data, after cloud screening (Sect. 2.4), to evaluate DOMNO v2,

516   QA4ECV, POMINO and POMINO v1.1. The scatterplots in Fig. 9a-d compare the NO_2

517   VCDs from 162 OMI pixels on 49 days with their MAX-DOAS counterparts. The

518   statistical results are shown in Table 2 as well. Different colors differentiate the seasons.

519   The high values of NO_2 VCD ($> 30 \times 10^{15}$ molec. cm^{-2}) occur mainly in fall (blue)

520   and winter (black). POMINO v1.1 and POMINO capture the day-to-day variability of

521   MAX-DOAS data, i.e., $R^2 = 0.80$ for both products. The normalized mean bias (NMB)

522   of POMINO v1.1 relative to MAX-DOAS data (-3.4%) is smaller than the NMB of

523   POMINO (-9.6%). Also, the reduced major axis (RMA) regression shows that the slope

524   for POMINO v1.1 (0.95) is closer to unity than the slope for POMINO (0.78). When

525   all OMI pixels in a day are averaged (Fig. 9e,f), the correlation across the total of 49

526   days further increase for both POMINO v1.1 ($R^2 = 0.89$) and POMINO ($R^2 = 0.86$),

527   whereas POMINO v1.1 still has a lower NMB (-3.7%) and better slope (0.96) than

528   POMINO (-10.4% and 0.82, respectively). These results suggest that correcting aerosol

529 vertical profiles, at least on a climatology basis, already leads to a significant improved

530 NO$_2$ retrieval from OMI.

531 Figure 9 show that DOMINO v2 is correlated with MAX-DOAS (R^2 = 0.68 in Fig. 9c

532 and 0.75 in Fig. 9g) but not as strong as POMINO and POMINO v1.1 for all days. The

533 discrepancy between DOMINO v2 and MAX-DOAS is particularly large for very high

534 NO$_2$ values (> 70 $\times$ 10^{15} molec. cm^{-2}). The R^2 for QA4ECV (0.75 in Fig. 9d and 0.82

535 in Fig. 9h) is slightly better than DOMINO, but the NMB is higher (-22.0% and -22.7%)

536 and the slope drops to 0.66. These results are consistent with the finding of Lin et al.

537 (2014b, 2015) that explicitly including aerosol optical effects improves the NO$_2$

538 retrieval.

539 Table 3 further shows the comparison statistics for 11 haze days. The haze days are

540 determined when both the ground meteorological station data and MODIS/Aqua

541 corrected reflectance (true color) data indicate a haze day. The table also lists AOD,

542 SSA, CF and MAX-DOAS NO$_2$ VCD, as averaged over all haze days. A large amount

543 of absorbing aerosols occurs on these haze days (AOD = 1.13, SSA = 0.90). The

544 average MAX-DOAS NO$_2$ VCD reaches 51.9 $\times$ 10^{15} molec. cm^{-2}. Among the four

545 satellite products, POMINO v1.1 has the highest R^2 (0.76) and the lowest bias (4.4%)

546 with respect to MAX-DOAS, whereas DOMINO v2 and QA4ECV reproduce the

547 variability to a limited extent (R^2 = 0.38 and 0.34, respectively). This is consistent with

548 the previous finding that the accuracy of DOMINO v2 is reduced for polluted, aerosol-

549 loaded scenes (Boersma et al., 2011; Chimot et al., 2016; Kanaya et al., 2014; Lin et

550 al., 2014b).

551 Table 4 shows the comparison statistics for 18 cloud-free days (CF = 0 in POMINO,

552 and AOD = 0.60 on average). Here, POMINO v1.1, POMINO and DONIMO v2 do not

553 show large differences in R^2 (0.53–0.56) and NMB (20.8–29.4%) with respect to MAX-

554 DOAS. QA4ECV has a higher R^2 (0.63) and a lower NMB (-5.8%), presumably

555 reflecting the improvements in this (EU-) consortium approach, at least in mostly cloud-
556 free situations. However, the R^2 values for POMINO and POMINO v1.1 are much
557 smaller than the R^2 values in haze days, whereas the opposite changes are true for
558 DOMINO v2 and QA4ECV. Thus, for this limited set of data, the changes from
559 DOMINO v2 and QA4ECV to POMINO and POMINO v1.1 mainly reflect the
560 improved aerosol treatment in hazy scenes. Further research may use additional MAX-
561 DOAS datasets to evaluate the satellite products more systematically.

562 **7. Conclusions**

563 This paper improves upon our previous POMINO algorithm (Lin et al., 2015) to retrieve
564 the tropospheric NO_2 VCDs from OMI, by compiling a 9-year (2007–2015) CALIOP
565 monthly climatology of aerosol vertical extinction profiles to adjust GEOS-Chem
566 aerosol profiles used in the NO_2 retrieval process. The improved algorithm is referred
567 to as POMINO v1.1. Compared to monthly climatological CALIOP data over China,
568 GEOS-Chem simulations tend to underestimate the aerosol extinction above 1 km, as
569 characterized by an underestimate in ALH by 300–600 m (seasonal and location
570 dependent). Such a bias is corrected in POMINO v1.1 by dividing, for any month and
571 grid cell, the CALIOP monthly climatological profile by the model climatological
572 profile to obtain a scaling profile and then applying the scaling profile to model data in
573 all days of that month in all years.

574 The aerosol extinction profile correction leads to an insignificant change in CF from
575 POMINO to POMINO v1.1, since the AOD and surface reflectance are unchanged. In
576 contrast, the correction results in a notably increase in CP (i.e., a decrease in CTH), due
577 to lifting of aerosol layers. The CP changes are generally within 6% for scenes with low
578 cloud fraction (CF < 0.05 in POMINO), and within 2% for scenes with modest cloud
579 fraction (0.2 < CF < 0.3 in POMINO).

580 The NO_2 VCDs increase from POMINO to POMINO v1.1 in most cases due to lifting

581 of aerosol layers that enhances the "shielding" of NO_2 absorption. The NO_2 VCD

582 increases by 3.4% (-67.5–41.7%) in spring for the domain average (range), 3.0% (-

583 59.5–34.4%) in summer, 4.6% (-15.3–39.6%) in fall and 5.3% (-68.4–49.3%) in winter.

584 The NO_2 changes highly season and location dependent, and are most significant for

585 wintertime Northern East China.

586 Further comparisons with independent MAX-DOAS NO_2 VCD data for 162 OMI

587 pixels in 49 days show good performance of both POMINO v1.1 and POMINO in

588 capturing the day-to-day variation of NO_2 (R^2=0.80, n=162), compared to DOMINO

589 v2 (R^2=0.67) and the new QA4ECV product (R^2=0.75). The NMB is smaller in

590 POMINO v1.1 (-3.4%) than in POMINO (-9.6%), with a slightly better slope (0.804

591 versus 0.784). On hazy days with high aerosol loadings (AOD = 1.13 on average),

592 POMINO v1.1 has the highest R^2 (0.76) and the lowest bias (4.4%) whereas DOMINO

593 and QA4ECV have difficulty in reproducing the day-to-day variability in MAX-DOAS

594 NO_2 measurements (R^2 = 0.38 and 0.34, respectively). The four products show small

595 differences in R^2 on clear-sky days (CF = 0 in POMINO, AOD = 0.60 on average),

596 among which QA4ECV shows a highest R^2 (0.63) and lowest NMB (-5.8%),

597 presumably reflecting the improvements in less polluted place such as Europe and the

598 US. Thus the explicit aerosol treatment (in POMINO and POMINO v1.1) and the

599 aerosol vertical profile correction (in POMINO v1.1) improves the NO_2 retrieval

600 especially in hazy cases.

601 The POMINO v1.1 algorithm is a core step towards our next public release of data

602 product, POMINO v2. The v2 product will contain a few additional updates, including

603 but not limited to using MODIS Collection 6 Merged 10-km Level-2 AOD data that

604 combine the Dark Target (Levy et al., 2013) and Deep Blue (Sayer et al., 2014) products,

605 as well as MODIS MCD43C2 Collection 6 daily BRDF data. Meanwhile, the POMINO

606 algorithm framework is being applied to the recently launched TropOMI instrument

607 that provides NO_2 information at a much higher spatial resolution (3.5 x 7 km^2). A

608 modified algorithm can also be used to retrieve sulfur dioxide, formaldehyde and other

609 trace gases from TropOMI, for which purposes our algorithm will be available to the

610 community on a collaborative basis. Future research can correct the SSA and NO_2

611 vertical profile to further improve the retrieval algorithm, and can use more

612 comprehensive independent data to evaluate the resulting satellite products.

Acknowledgements

613

614 This research is supported by the National Natural Science Foundation of China

615 (41775115), the 973 program (2014CB441303), the Chinese Scholarship Council, and

616 the EU FP7 QA4ECV project (grant no. 607405).

Appendix A: Introduction to the QA4ECV product

617

618 The QA4ECV NO_2 product (http://www.qa4ecv.eu/) builds on a (EU-) consortium

619 approach to retrieve NO_2 from GOME, SCIAMACHY, GOME-2, and OMI. The main

620 contributions are provided by BIRA-IASB, the University of Bremen (IUP), MPIC,

621 KNMI, and Wageningen University. Uncertainties in spectral fitting for NO_2 SCDs and

622 in AMF calculations were evaluated by Zara et al. (2018) and Lorente et al. (2017),

623 respectively. QA4ECV contains improved SCD NO_2 data (Zara et al., 2018). Our test

624 suggests that using the QA4ECV SCD data instead of DOMINO SCD data would

625 reduce the underestimate against MAX-DOAS VCD data from 3.7% to 0.2%, a relative

626 minor improvement. Lorente et al., (2017) showed that across the above algorithms,

627 there a structural uncertainty by 42% in the NO_2 AMF calculation over polluted areas.

628 By comparing to our POMINO product, Lorente et al. also showed that the choice of

629 aerosol correction may introduce an additional uncertainty by up to 50% for situations

630 with high polluted cases, consistent with Lin et al. (2014b, 2015) and the findings here.

631   For a complete description of the QA4ECV algorithm improvements, and quality

632   assurance, please see Boersma et al. (2018).

Appendix B: Constructing the CALIOP monthly climatology of aerosol extinction

634   **vertical profile**

635   Our use the all-sky Level-2 CALIOP data to construct the Level-3 monthly climatology.

636   We choose the all-sky product instead of clear-sky data, since previous studies indicate

637   that the climatological aerosol extinction profiles are affected insignificantly by the

638   presence of clouds (Koffi et al., 2012; Winker et al., 2013). As we use this

639   climatological data to adjust GEOS-Chem results, choosing all-sky data improves

640   consistency with the model simulation when doing the daily correction.

641   To select valid pixels, we follow the data quality criteria by Winker et al., (2013) and

642   Amiridis et al., (2015). Only the pixels with Cloud Aerosol Discrimination (CAD)

643   scores between -20 and -100 with extinction Quality Control (QC) flag valued at 0, 1,

644   18, and 16 are selected. We further discard samples with an extinction uncertainty of

645   99.9 km^{-1}, which is indicative of unreliable retrieval. We only accept extinction values

646   falling in the range from 0.0 to 1.25, according to CALIOP observation thresholds.

647   Previous studies showed that weakly scattering edges of icy clouds are sometimes

648   misclassified as aerosols (Winker et al., 2013). To eliminate contamination from icy

649   clouds we exclude the aerosol layers above the cloud layer (with layer-top temperature

650   below 0 ℃) when both of them are above 4km (Winker et al., 2013).

651   After the pixel-based screening, we aggregate the CALIOP data at the model grid

652   (0.667^0 long. x 0.5^0 lat.) and vertical resolution (47 layers, with 36 layers or so in the

653   troposphere). For each grid cell, we choose the CALIOP pixels within 1.5^0 of the grid

654   cell center. CALIOP Level-2 data are always presented at the fixed 399 altitudes above

655   sea level. To account for the difference in surface elevation between a CALIOP pixel

656   and the respective model grid cell, we convert the altitude of the pixel to a height above

657   the ground, by using the surface elevation data provided in CALIOP. We then average

658   horizontally and vertically the profiles of all pixels within one model grid cell and layer.

659   We do the regridding day-by-day for all grid cells to ensure that GEOS-Chem and

660   CALIOP extinction profiles are coincident spatially and temporally. Finally, we

661   compile a monthly climatological dataset by averaging over 2007–2015.

662   Figure A1 shows the number of aerosol extinction profiles in each grid cell and 12 x 9

663   = 108 months that are used to compile the CALIOP climatology, both before and after

664   data screening. Table A1 presents additional information on monthly and yearly bases.

665   On average, there are 165 and 47 aerosol extinction profiles per month per grid cell

666   before and after screening, respectively. In the final 9-year monthly climatology, each

667   grid cell has about 420 aerosol extinction profiles on average, about 28% of the prior-

668   screening profiles. Figure A1 shows that the number of valid profiles decreases sharply

669   over the Tibet Plateau and at higher latitudes ($> 43\ ^{\circ}$ N) due to complex terrain and

670   icy/snowy ground.

671   As discussed above, we choose the CALIOP pixels within 1.5° of a grid cell center.

672   We test this choice by examining the aerosol layer height (ALH) produced for that grid

673   cell. The ALH is defined as the extinction-weighted height of aerosols (see Eq. A1,

674   where n denotes the number of tropospheric layers, ε_i the aerosol extinction at layer

675   i, and H_i the layer center height above the ground). We find that choosing pixels

676   within 1.0° of a grid cell center leads to a nosier horizontal distribution of ALH, owing

677   to the small footprint of CALIOP. On the other hand, choosing 2.0^0 leads to a too

678   smooth spatial gradient of ALH with local characteristics of aerosol vertical

679   distributions are largely lost. We thus decide that 1.5^0 is a good balance between noise

680   and smoothness.

681     $ALH = \frac{\sum_{i=1}^{i=n} \varepsilon_i H_i}{\sum_{i=1}^{i=n} \varepsilon_i}$ (A1)

682   Certain grid cells do not contain sufficient valid observations for some months of the

683   climatological dataset. We fill in missing monthly values of a grid cell using valid data

684   in the surrounding 5 x 5 = 25 grid cells (within ~ 100 km). If the 25 grid cells do not

685   have enough valid data, we use those in the surrounding 7 x 7 = 49 grid cells (within ~

686   150 km). A similar procedure is used by Lin et al. (2014b, 2015) to fill in missing values

687   in the gridded MODIS AOD dataset.

688   For each grid cell in each month, we further correct singular values in the vertical profile.

689   In a month, if a grid cell i has an ALH outside mean$\pm 1\sigma$ of its surrounding 25 or 49

690   grid cells, we select i's surrounding grid cell j whose ALH is the median of i's

691   surrounding grid cells, and use j's profile to replace i's. Whether 25 or 49 surrounding

692   grid cells are chosen depends on the number of valid pixels shown in Fig. A1b. If the

693   number of valid pixels in i is below mean-1σ of all grid cells in the whole domain,

694   which is often the case for Tibetan grid cells, we use i's surrounding 49 grid cells;

695   otherwise we use i's surrounding 25 grid cells.

696   **Appendix C. Comparing our and NASA's CALIOP monthly climatology**

697   We compare our gridded climatological profiles to NASA CALIOP Version 3 Level-3

698   all-sky monthly profiles at 532 nm (Winker et al., 2013). The NASA Level-3 data has

699   a horizontal resolution of 2^0 lat. $\times$ 5^0 lon. and a vertical resolution of 60 m (from -0.5

700   to 12 km above sea level). We combine NASA monthly data over 2007–2015 to

701   construct a monthly climatology for comparison with our own compilation. We only

702   choose aerosol extinction data in the troposphere with error less than 0.15 (the valid

703   range given in the CALIOP dataset). If the number of valid monthly profiles in a grid

704   cell is less than five (i.e., for the same month in five out of the nine years), then we

705   exclude data in that grid cell; see the dark gray grid cells in Fig. 2c.

706 Several methodological differences exist between generating our and NASA CALIOP

707 datasets. First, the two datasets have different horizontal resolutions. Also, we sample

708 all valid CALIOP pixels within 1.5^0 of a grid cell center, whereas the NASA dataset

709 samples all valid pixels within a grid cell. Besides, our CALIOP dataset involves

710 several steps of horizontal interpolation, for purposes of subsequent cloud and NO_2

711 retrievals, which is not done in the NASA dataset. In addition, we match CALIOP data

712 vertically to the GEOS-Chem vertical resolution, whereas the NASA dataset maintains

713 the original resolution.

714 Figure 2c shows the spatial distribution of ALH in all seasons based on NASA CALIOP

715 Level-3 all-sky monthly climatology. The horizontal resolution of NASA data is much

716 coarser than ours; and NASA data are largely missing over the southwest with complex

717 terrains. We choose to focus on the comparison over East China (the black box in Fig.

718 1a). Over East China, the two climatology datasets generally exhibit similar spatial

719 patterns of ALH in all seasons (Fig. 2a, c). The NASA dataset suggests higher ALHs

720 than ours over Eastern China, especially in summer, due mainly to differences in the

721 sampling and regridding processes. Figure 3c further compares the monthly variation

722 of ALH between our (black line with error bars) and NASA (blue filled triangles)

723 datasets averaged over East China. The two datasets are consistent in almost all months,

724 indicating that their regional differences are largely smoothed out by spatial averaging.

725 **References**

726 Acarreta, J. R., De Haan, J. F. and Stammes, P.: Cloud pressure retrieval using the O_2 -

727 O_2 absorption band at 477 nm, J. Geophys. Res., 109(D5), D05204,

728 doi:10.1029/2003JD003915, 2004.

729 Amiridis, V., Marinou, E., Tsekeri, A., Wandinger, U., Schwarz, A., Giannakaki, E.,

730 Mamouri, R., Kokkalis, P., Binietoglou, I., Solomos, S., Herekakis, T., Kazadzis, S.,

731   Gerasopoulos, E., Proestakis, E., Kottas, M., Balis, D., Papayannis, A., Kontoes, C.,

732   Kourtidis, K., Papagiannopoulos, N., Mona, L., Pappalardo, G., Le Rille, O. and

733   Ansmann, A.: LIVAS: a 3-D multi-wavelength aerosol/cloud database based on

734   CALIPSO and EARLINET, Atmos. Chem. Phys., 15(13), 7127–7153,

735   doi:10.5194/acp-15-7127-2015, 2015.

736   Belmonte Rivas, M., Veefkind, P., Boersma, F., Levelt, P., Eskes, H. and Gille, J.:

737   Intercomparison of daytime stratospheric NO_2 satellite retrievals and model simulations,

738   Atmos. Meas. Tech., 7(7), 2203–2225, doi:10.5194/amt-7-2203-2014, 2014.

739   Boersma, K. F., Eskes, H. J. and Brinksma, E. J.: Error analysis for tropospheric NO_2

740   retrieval from space, J. Geophys. Res. Atmos., 109(D4), n/a-n/a,

741   doi:10.1029/2003JD003962, 2004.

742   Boersma, K. F., Eskes, H. J., Veefkind, J. P., Brinksma, E. J., van der A, R. J., Sneep,

743   M., van den Oord, G. H. J., Levelt, P. F., Stammes, P., Gleason, J. F. and Bucsela, E.

744   J.: Near-real time retrieval of tropospheric NO_2 from OMI, Atmos. Chem. Phys., 7(8),

745   2103–2118, doi:10.5194/acp-7-2103-2007, 2007.

746   Boersma, K. F., Eskes, H. J., Dirksen, R. J., van der A, R. J., Veefkind, J. P., Stammes,

747   P., Huijnen, V., Kleipool, Q. L., Sneep, M., Claas, J., Leitão, J., Richter, A., Zhou, Y.

748   and Brunner, D.: An improved tropospheric NO_2 column retrieval algorithm for the

749   Ozone Monitoring Instrument, Atmos. Meas. Tech., 4(9), 1905–1928,

750   doi:10.5194/amt-4-1905-2011, 2011.

751   Boersma, K. F., Eskes, H. J., Richter, A., De Smedt, I., Lorente, A., Beirle, S., van

752   Geffen, J. H. G. M., Zara, M., Peters, E., Van Roozendael, M., Wagner, T., Maasakkers,

753   J. D., van der A, R. J., Nightingale, J., De Rudder, A., Irie, H., Pinardi, G., Lambert, J.-

754   C., and Compernolle, S.: Improving algorithms and uncertainty estimates for satellite

755   NO_2 retrievals: Results from the Quality Assurance for Essential Climate Variables

756 (QA4ECV) project, Atmos. Meas. Tech. Discuss., https://doi.org/10.5194/amt-2018-
757 200, in review, 2018.

758 Bucsela, E. J., Celarier, E. A., Wenig, M. O., Gleason, J. F., Veefkind, J. P., Boersma,
759 K. F. and Brinksma, E. J.: Algorithm for NO_2 vertical column retrieval from the ozone
760 monitoring instrument, IEEE Trans. Geosci. Remote Sens., 44(5), 1245–1258,
761 doi:10.1109/TGRS.2005.863715, 2006.

762 Bucsela, E. J., Krotkov, N. A., Celarier, E. A., Lamsal, L. N., Swartz, W. H., Bhartia,
763 P. K., Boersma, K. F., Veefkind, J. P., Gleason, J. F. and Pickering, K. E.: A new
764 stratospheric and tropospheric NO_2 retrieval algorithm for nadir-viewing satellite
765 instruments: applications to OMI, Atmos. Meas. Tech., 6(10), 2607–2626,
766 doi:10.5194/amt-6-2607-2013, 2013.

767 Castellanos, P., Boersma, K. F. and van der Werf, G. R.: Satellite observations indicate
768 substantial spatiotemporal variability in biomass burning NO_X emission factors for
769 South America, Atmos. Chem. Phys., 14(8), 3929–3943, doi:10.5194/acp-14-3929-
770 2014, 2014.

771 Castellanos, P., Boersma, K. F., Torres, O. and de Haan, J. F.: OMI tropospheric NO_2
772 air mass factors over South America: effects of biomass burning aerosols, Atmos. Meas.
773 Tech., 8(9), 3831–3849, doi:10.5194/amt-8-3831-2015, 2015.

774 Chazette, P., Raut, J.-C., Dulac, F., Berthier, S., Kim, S.-W., Royer, P., Sanak, J., Loaëc,
775 S. and Grigaut-Desbrosses, H.: Simultaneous observations of lower tropospheric
776 continental aerosols with a ground-based, an airborne, and the spaceborne CALIOP
777 lidar system, J. Geophys. Res., 115(D4), D00H31, doi:10.1029/2009JD012341, 2010.

778 Chimot, J., Vlemmix, T., Veefkind, J. P., de Haan, J. F. and Levelt, P. F.: Impact of
779 aerosols on the OMI tropospheric NO_2 retrievals over industrialized regions: how

780 accurate is the aerosol correction of cloud-free scenes via a simple cloud model?,

781 Atmos. Meas. Tech., 9(2), 359–382, doi:10.5194/amt-9-359-2016, 2016.

782 Clémer, K., Van Roozendael, M., Fayt, C., Hendrick, F., Hermans, C., Pinardi, G.,

783 Spurr, R., Wang, P. and De Mazière, M.: Multiple wavelength retrieval of tropospheric

784 aerosol optical properties from MAX-DOAS measurements in Beijing, Atmos. Meas.

785 Tech., 3(4), 863–878, doi:10.5194/amt-3-863-2010, 2010.

786 Cui, Y., Lin, J., Song, C., Liu, M., Yan, Y., Xu, Y. and Huang, B.: Rapid growth in

787 nitrogen dioxide pollution over Western China, 2005–2013, Atmos. Chem. Phys.,

788 16(10), 6207–6221, doi:10.5194/acp-16-6207-2016, 2016.

789 Dirksen, R. J., Boersma, K. F., Eskes, H. J., Ionov, D. V., Bucsela, E. J., Levelt, P. F.

790 and Kelder, H. M.: Evaluation of stratospheric NO_2 retrieved from the Ozone

791 Monitoring Instrument: Intercomparison, diurnal cycle, and trending, J. Geophys. Res.,

792 116(D8), D08305, doi:10.1029/2010JD014943, 2011.

793 van Geffen, J. H. G. M., Boersma, K. F., Van Roozendael, M., Hendrick, F., Mahieu,

794 E., De Smedt, I., Sneep, M. and Veefkind, J. P.: Improved spectral fitting of nitrogen

795 dioxide from OMI in the 405–465 nm window, Atmos. Meas. Tech., 8(4), 1685–1699,

796 doi:10.5194/amt-8-1685-2015, 2015.

797 Gielen, C., Van Roozendael, M., Hendrick, F., Pinardi, G., Vlemmix, T., De Bock, V.,

798 De Backer, H., Fayt, C., Hermans, C., Gillotay, D. and Wang, P.: A simple and versatile

799 cloud-screening method for MAX-DOAS retrievals, Atmos. Meas. Tech., 7(10), 3509–

800 3527, doi:10.5194/amt-7-3509-2014, 2014.

801 Hendrick, F., Muller, J. F., Clemer, K., Wang, P., De Maziere, M., Fayt, C., Gielen, C.,

802 Hermans, C., Ma, J. Z., Pinardi, G., Stavrakou, T., Vlemmix, T., and Van Roozendael,

803 M.: Four years of ground-based MAX-DOAS observations of HONO and NO_2 in the

804 Beijing area, Atmospheric Chemistry and Physics, 14, 765-781, 10.5194/acp-14-765-
805 2014, 2014.

806 Huang, Z., Huang, J., Bi, J., Wang, G., Wang, W., Fu, Q., Li, Z., Tsay, S.-C. and Shi,
807 J.: Dust aerosol vertical structure measurements using three MPL lidars during 2008
808 China-U.S. joint dust field experiment, J. Geophys. Res. Atmos., 115(D7), n/a-n/a,
809 doi:10.1029/2009JD013273, 2010.

810 Irie, H., Boersma, K. F., Kanaya, Y., Takashima, H., Pan, X. and Wang, Z. F.:
811 Quantitative bias estimates for tropospheric NO_2 columns retrieved from
812 SCIAMACHY, OMI, and GOME-2 using a common standard for East Asia, Atmos.
813 Meas. Tech., 5(10), 2403–2411, doi:10.5194/amt-5-2403-2012, 2012.

814 Jethva, H., Torres, O., and Ahn, C.: A ten-year global record of absorbing aerosols
815 above clouds from OMI's near-UV observations, in: Remote Sensing of the Atmosphere,
816 Clouds, and Precipitation Vi, edited by: Im, E., Kumar, R., and Yang, S., Proceedings
817 of SPIE, 2016.

818 Johnson, M. S., Meskhidze, N. and Praju Kiliyanpilakkil, V.: A global comparison of
819 GEOS-Chem-predicted and remotely-sensed mineral dust aerosol optical depth and
820 extinction profiles, J. Adv. Model. Earth Syst., 4(3), M07001,
821 doi:10.1029/2011MS000109, 2012.

822 Kacenelenbogen, M., Redemann, J., Vaughan, M. A., Omar, A. H., Russell, P. B.,
823 Burton, S., Rogers, R. R., Ferrare, R. A. and Hostetler, C. A.: An evaluation of
824 CALIOP/CALIPSO's aerosol-above-cloud detection and retrieval capability over
825 North America, J. Geophys. Res. Atmos., 119(1), 230–244,
826 doi:10.1002/2013JD020178, 2014.

827 Kanaya, Y., Irie, H., Takashima, H., Iwabuchi, H., Akimoto, H., Sudo, K., Gu, M.,
828 Chong, J., Kim, Y. J., Lee, H., Li, A., Si, F., Xu, J., Xie, P.-H., Liu, W.-Q., Dzhola, A.,

829   Postylyakov, O., Ivanov, V., Grechko, E., Terpugova, S. and Panchenko, M.: Long-
830   term MAX-DOAS network observations of NO_2 in Russia and Asia (MADRAS) during
831   the period 2007-2012: instrumentation, elucidation of climatology, and comparisons
832   with OMI satellite observations and global model simulations, Atmos. Chem. Phys.,
833   14(15), 7909–7927, doi:10.5194/acp-14-7909-2014, 2014.

834   Kim, S.-W., Heckel, A., Frost, G. J., Richter, A., Gleason, J., Burrows, J. P., McKeen,
835   S., Hsie, E.-Y., Granier, C. and Trainer, M.: NO_2 columns in the western United States
836   observed from space and simulated by a regional chemistry model and their
837   implications for NO_x emissions, J. Geophys. Res., 114(D11), D11301,
838   doi:10.1029/2008JD011343, 2009.

839   Koffi, B., Schulz, M., Bréon, F.-M., Griesfeller, J., Winker, D., Balkanski, Y., Bauer,
840   S., Berntsen, T., Chin, M., Collins, W. D., Dentener, F., Diehl, T., Easter, R., Ghan, S.,
841   Ginoux, P., Gong, S., Horowitz, L. W., Iversen, T., Kirkevåg, A., Koch, D., Krol, M.,
842   Myhre, G., Stier, P. and Takemura, T.: Application of the CALIOP layer product to
843   evaluate the vertical distribution of aerosols estimated by global models: AeroCom
844   phase I results, J. Geophys. Res. Atmos., 117(D10), n/a-n/a,
845   doi:10.1029/2011JD016858, 2012.

846   Leitão, J., Richter, A., Vrekoussis, M., Kokhanovsky, A., Zhang, Q. J., Beekmann, M.
847   and Burrows, J. P.: On the improvement of NO_2 satellite retrievals – aerosol impact on
848   the airmass factors, Atmos. Meas. Tech., 3(2), 475–493, doi:10.5194/amt-3-475-2010,
849   2010.

850   Lerot, C., Stavrakou, T., De Smedt, I., Müller, J.-F. and Van Roozendael, M.: Glyoxal
851   vertical columns from GOME-2 backscattered light measurements and comparisons
852   with a global model, Atmos. Chem. Phys., 10(24), 12059–12072, doi:10.5194/acp-10-
853   12059-2010, 2010.

854 Levy, R. C., Mattoo, S., Munchak, L. A., Remer, L. A., Sayer, A. M., Patadia, F. and

855 Hsu, N. C.: The Collection 6 MODIS aerosol products over land and ocean, Atmos.

856 Meas. Tech., 6(11), 2989–3034, doi:10.5194/amt-6-2989-2013, 2013.

857 Li, S., Yu, C., Chen, L., Tao, J., Letu, H., Ge, W., Si, Y. and Liu, Y.: Inter-comparison

858 of model-simulated and satellite-retrieved componental aerosol optical depths in China,

859 Atmos. Environ., 141, 320–332, doi:https://doi.org/10.1016/j.atmosenv.2016.06.075,

860 2016.

861 Lin, J., Pan, D., Davis, S. J., Zhang, Q., He, K., Wang, C., Streets, D. G., Wuebbles, D.

862 J. and Guan, D.: China's international trade and air pollution in the United States, Proc.

863 Natl. Acad. Sci., 111(5), 1736–1741, doi:10.1073/pnas.1312860111, 2014a.

864 Lin, J.-T.: Satellite constraint for emissions of nitrogen oxides from anthropogenic,

865 lightning and soil sources over East China on a high-resolution grid, Atmos. Chem.

866 Phys., 12(6), 2881–2898, doi:10.5194/acp-12-2881-2012, 2012.

867 Lin, J.-T., McElroy, M. B. and Boersma, K. F.: Constraint of anthropogenic NO_X

868 emissions in China from different sectors: a new methodology using multiple satellite

869 retrievals, Atmos. Chem. Phys., 10(1), 63–78, doi:10.5194/acp-10-63-2010, 2010.

870 Lin, J.-T., Martin, R. V., Boersma, K. F., Sneep, M., Stammes, P., Spurr, R., Wang, P.,

871 Van Roozendael, M., Clémer, K. and Irie, H.: Retrieving tropospheric nitrogen dioxide

872 from the Ozone Monitoring Instrument: effects of aerosols, surface reflectance

873 anisotropy, and vertical profile of nitrogen dioxide, Atmos. Chem. Phys., 14(3), 1441–

874 1461, doi:10.5194/acp-14-1441-2014, 2014b.

875 Lin, J.-T., Liu, M.-Y., Xin, J.-Y., Boersma, K. F., Spurr, R., Martin, R. and Zhang, Q.:

876 Influence of aerosols and surface reflectance on satellite NO_2 retrieval: seasonal and

877 spatial characteristics and implications for NO_x emission constraints, Atmos. Chem.

878 Phys., 15(19), 11217–11241, doi:10.5194/acp-15-11217-2015, 2015.

879   Lorente, A., Folkert Boersma, K., Yu, H., Dörner, S., Hilboll, A., Richter, A., Liu, M.,

880   Lamsal, L. N., Barkley, M., De Smedt, I., Van Roozendael, M., Wang, Y., Wagner, T.,

881   Beirle, S., Lin, J.-T., Krotkov, N., Stammes, P., Wang, P., Eskes, H. J. and Krol, M.:

882   Structural uncertainty in air mass factor calculation for NO_2 and HCHO satellite

883   retrievals, Atmos. Meas. Tech., 10(3), 759–782, doi:10.5194/amt-10-759-2017, 2017.

884   Lucht, W., Schaaf, C. B. and Strahler, A. H.: An algorithm for the retrieval of albedo

885   from space using semiempirical BRDF models, IEEE Trans. Geosci. Remote Sens.,

886   38(2), 977–998, doi:10.1109/36.841980, 2000.

887   Ma, J. Z., Beirle, S., Jin, J. L., Shaiganfar, R., Yan, P. and Wagner, T.: Tropospheric

888   NO_2 vertical column densities over Beijing: results of the first three years of ground-

889   based MAX-DOAS measurements (2008-2011) and satellite validation, Atmos. Chem.

890   Phys., 13(3), 1547–1567, doi:10.5194/acp-13-1547-2013, 2013.

891   Ma, X. and Yu, F.: Seasonal variability of aerosol vertical profiles over east US and

892   west Europe: GEOS-Chem/APM simulation and comparison with CALIPSO

893   observations,   Atmos.   Res.,   140–141,   28–37,

894   doi:https://doi.org/10.1016/j.atmosres.2014.01.001, 2014.

895   Martin, R. V.: An improved retrieval of tropospheric nitrogen dioxide from GOME, J.

896   Geophys. Res., 107(D20), 4437, doi:10.1029/2001JD001027, 2002.

897   Misra, A., Tripathi, S. N., Kaul, D. S. and Welton, E. J.: Study of MPLNET-Derived

898   Aerosol Climatology over Kanpur, India, and Validation of CALIPSO Level 2 Version

899   3 Backscatter and Extinction Products, J. Atmos. Ocean. Technol., 29(9), 1285–1294,

900   doi:10.1175/JTECH-D-11-00162.1, 2012.

901   Miyazaki, K. and Eskes, H.: Constraints on surface NO_X emissions by assimilating

902   satellite observations of multiple species, Geophys. Res. Lett., 40(17), 4745–4750,

903   doi:10.1002/grl.50894, 2013.

904 Proestakis, E., Amiridis, V., Marinou, E., Georgoulias, A. K., Solomos, S., Kazadzis,

905 S., Chimot, J., Che, H., Alexandri, G., Binietoglou, I., Kourtidis, K. A., de Leeuw, G.

906 and van der A, R. J.: 9-year spatial and temporal evolution of desert dust aerosols over

907 South-East Asia as revealed by CALIOP, Atmos. Chem. Phys. Discuss., 1–35,

908 doi:10.5194/acp-2017-797, 2017.

909 Richter, A., Begoin, M., Hilboll, A. and Burrows, J. P.: An improved NO_2 retrieval for

910 the GOME-2 satellite instrument, Atmos. Meas. Tech., 4(6), 1147–1159,

911 doi:10.5194/amt-4-1147-2011, 2011.

912 Marchenko, S., Krotkov, N. A., Lamsal, L. N., Celarier, E. A., Swartz, W. H.,

913 and Bucsela, E. J.: Revising the slant column density retrieval of nitrogen dioxide

914 observed by the Ozone Monitoring Instrument, J. Geophys. Res. Atmos., 120(11),

915 5670–5692, doi:10.1002/2014JD022913, 2015.

916 Sareen, N., Schwier, A. N., Shapiro, E. L., Mitroo, D. and McNeill, V. F.: Secondary

917 organic material formed by methylglyoxal in aqueous aerosol mimics, Atmos. Chem.

918 Phys., 10(3), 997–1016, doi:10.5194/acp-10-997-2010, 2010.

919 Sayer, A. M., Munchak, L. A., Hsu, N. C., Levy, R. C., Bettenhausen, C. and Jeong,

920 M.-J.: MODIS Collection 6 aerosol products: Comparison between Aqua's e-Deep

921 Blue, Dark Target, and "merged" data sets, and usage recommendations, J. Geophys.

922 Res. Atmos., 119(24), 13,965-13,989, doi:10.1002/2014JD022453, 2014.

923 Schenkeveld, V. M. E., Jaross, G., Marchenko, S., Haffner, D., Kleipool, Q. L.,

924 Rozemeijer, N. C., Veefkind, J. P., and Levelt, P. F.: In-flight performance of the Ozone

925 Monitoring Instrument, Atmospheric Measurement Techniques, 10, 1957-1986,

926 10.5194/amt-10-1957-2017, 2017.

927 Stammes, P., Sneep, M., de Haan, J. F., Veefkind, J. P., Wang, P. and Levelt, P. F.:

928 Effective cloud fractions from the Ozone Monitoring Instrument: Theoretical

929 framework and validation, J. Geophys. Res., 113(D16), D16S38,
930 doi:10.1029/2007JD008820, 2008.

931 Stavrakou, T., Müller, J.-F., Bauwens, M., De Smedt, I., Lerot, C., Van Roozendael,
932 M., Coheur, P.-F., Clerbaux, C., Boersma, K. F., van der A, R. and Song, Y.: Substantial
933 Underestimation of Post-Harvest Burning Emissions in the North China Plain Revealed
934 by Multi-Species Space Observations, Sci. Rep., 6, 32307, doi:10.1038/srep32307,
935 2016.

936 van Donkelaar, A., Martin, R. V., Spurr, R. J. D., Drury, E., Remer, L. A., Levy, R. C.,
937 and Wang, J.: Optimal estimation for global ground-level fine particulate matter
938 concentrations, Journal of Geophysical Research-Atmospheres, 118, 5621-5636,
939 10.1002/jgrd.50479, 2013.

940 Veefkind, J. P., de Haan, J. F., Sneep, M. and Levelt, P. F.: Improvements to the OMI
941 O_2-O_2 operational cloud algorithm and comparisons with ground-based radar–lidar
942 observations, Atmos. Meas. Tech., 9(12), 6035–6049, doi:10.5194/amt-9-6035-2016,
943 2016.

944 Verstraeten, W. W., Neu, J. L., Williams, J. E., Bowman, K. W., Worden, J. R. and
945 Boersma, K. F.: Rapid increases in tropospheric ozone production and export from
946 China, Nat. Geosci., 8, 690 [online] Available from:
947 http://dx.doi.org/10.1038/ngeo2493, 2015.

948 Wang, J., Jacob, D. J. and Martin, S. T.: Sensitivity of sulfate direct climate forcing to
949 the hysteresis of particle phase transitions, J. Geophys. Res. Atmos., 113(D11), n/a-n/a,
950 doi:10.1029/2007JD009368, 2008a.

951 Wang, M., Gu, J., Yang, R., Zeng, L. and Wang, S.: Comparison of cloud type and
952 frequency over China from surface, FY-2E, and CloudSat observations, vol. 9259, pp.
953 925913–925914. [online] Available from: http://dx.doi.org/10.1117/12.2069110, 2014.

954   Wang, P. and Stammes, P.: Evaluation of SCIAMACHY Oxygen A band cloud heights

955   using Cloudnet measurements, Atmos. Meas. Tech., 7(5), 1331–1350,

956   doi:10.5194/amt-7-1331-2014, 2014.

957   Wang, P., Stammes, P., van der A, R., Pinardi, G. and van Roozendael, M.: FRESCO+:

958   an improved O_2 A-band cloud retrieval algorithm for tropospheric trace gas retrievals,

959   Atmos. Chem. Phys., 8(21), 6565–6576, doi:10.5194/acp-8-6565-2008, 2008b.

960   Wang, X., Huang, J., Zhang, R., Chen, B. and Bi, J.: Surface measurements of aerosol

961   properties over northwest China during ARM China 2008 deployment, J. Geophys. Res.

962   Atmos., 115(D7), n/a-n/a, doi:10.1029/2009JD013467, 2010.

963   Wang, Y., Penning de Vries, M., Xie, P. H., Beirle, S., Dörner, S., Remmers, J., Li, A.

964   and Wagner, T.: Cloud and aerosol classification for 2.5 years of MAX-DOAS

965   observations in Wuxi (China) and comparison to independent data sets, Atmos. Meas.

966   Tech., 8(12), 5133–5156, doi:10.5194/amt-8-5133-2015, 2015.

967   Wang, Y., Lampel, J., Xie, P., Beirle, S., Li, A., Wu, D. and Wagner, T.: Ground-based

968   MAX-DOAS observations of tropospheric aerosols, NO_2, SO_2 and HCHO in Wuxi,

969   China, from 2011 to 2014, Atmos. Chem. Phys., 17(3), 2189–2215, doi:10.5194/acp-

970   17-2189-2017, 2017a.

971   Wang, Y., Beirle, S., Lampel, J., Koukouli, M., De Smedt, I., Theys, N., Li, A., Wu,

972   D., Xie, P., Liu, C., Van Roozendael, M., Stavrakou, T., Müller, J.-F. and Wagner, T.:

973   Validation of OMI, GOME-2A and GOME-2B tropospheric NO_2, SO_2 and HCHO

974   products using MAX-DOAS observations from 2011 to 2014 in Wuxi, China:

975   investigation of the effects of priori profiles and aerosols on the satellite products,

976   Atmos. Chem. Phys., 17(8), 5007–5033, doi:10.5194/acp-17-5007-2017, 2017b.

977   Winker, D. M., Pelon, J., Coakley, J. A., Ackerman, S. A., Charlson, R. J., Colarco, P.

978   R., Flamant, P., Fu, Q., Hoff, R. M., Kittaka, C., Kubar, T. L., Le Treut, H., Mccormick,

979 M. P., Mégie, G., Poole, L., Powell, K., Trepte, C., Vaughan, M. A. and Wielicki, B.

980 A.: The CALIPSO Mission, Bull. Am. Meteorol. Soc., 91(9), 1211–1230,

981 doi:10.1175/2010BAMS3009.1, 2010.

982 Winker, D. M., Tackett, J. L., Getzewich, B. J., Liu, Z., Vaughan, M. A. and Rogers,

983 R. R.: The global 3-D distribution of tropospheric aerosols as characterized by CALIOP,

984 Atmos. Chem. Phys., 13(6), 3345–3361, doi:10.5194/acp-13-3345-2013, 2013.

985 Zara, M., Boersma, K. F., De Smedt, I., Richter, A., Peters, E., Van Geffen, J. H. G. M.,

986 Beirle, S., Wagner, T., Van Roozendael, M., Marchenko, S., Lamsal, L. N. and Eskes,

987 H. J.: Improved slant column density retrieval of nitrogen dioxide and formaldehyde

988 for OMI and GOME-2A from QA4ECV: intercomparison, uncertainty characterization,

989 and trends, Atmos. Meas. Tech. Discuss., 1–47, doi:10.5194/amt-2017-453, 2018.

990 Zhang, Q., Streets, D. G., Carmichael, G. R., He, K. B., Huo, H., Kannari, A., Klimont,

991 Z., Park, I. S., Reddy, S., Fu, J. S., Chen, D., Duan, L., Lei, Y., Wang, L. T. and Yao,

992 Z. L.: Asian emissions in 2006 for the NASA INTEX-B mission, Atmos. Chem. Phys.,

993 9(14), 5131–5153, doi:10.5194/acp-9-5131-2009, 2009.

994 Zhao, C. and Wang, Y.: Assimilated inversion of NO_X emissions over east Asia using

995 OMI NO_2 column measurements, Geophys. Res. Lett., 36(6), L06805,

996 doi:10.1029/2008GL037123, 2009.

997 Zhao, H. Y., Zhang, Q., Guan, D. B., Davis, S. J., Liu, Z., Huo, H., Lin, J. T., Liu, W.

998 D. and He, K. B.: Assessment of China's virtual air pollution transport embodied in

999 trade by using a consumption-based emission inventory, Atmos. Chem. Phys., 15(10),

1000 5443–5456, doi:10.5194/acp-15-5443-2015, 2015.

1001 Zhou, Y., Brunner, D., Spurr, R. J. D., Boersma, K. F., Sneep, M., Popp, C. and

1002 Buchmann, B.: Accounting for surface reflectance anisotropy in satellite retrievals of

1003   tropospheric NO_2, Atmos. Meas. Tech., 3(5), 1185–1203, doi:10.5194/amt-3-1185-

1004   2010, 2010.

1005   Zhu, W., Xu, C., Qian, X. and Wei, H.: Statistical analysis of the spatial-temporal

1006   distribution of aerosol extinction retrieved by micro-pulse lidar in Kashgar, China, Opt.

1007   Express, 21(3), 2531–2537, doi:10.1364/OE.21.002531, 2013.

1008

1009

Table A1. Number of CALIOP observations in a grid cell ($0.667^0 \times 0.5^0$).

	Before filtering				After filtering			
	Mean	Median	Minima	Maximum	Mean	Median	Minima	Maximum
For a month	165	169	0	291	47	39	0	223
For the same month in nine years	1483	1513	192	1921	420	395	0	1548
For all months in nine years	17794	18528	5608	20781	5033	5381	146	12650

1010

Table 1. MAX-DOAS measurement sites and corresponding meteorological stations.

MAX-DOAS site name	Site information	Measurement times	Corresponding meteorological station name	Meteorological station information
Xianghe	116.96^{o}E, 39.75^{o}N, 36 m, suburban	2012/01/01 -2012/12/31	CAPITAL INTERNATIONA	116.89^{o}E, 40.01^{o}N, 35.4 m
IAP	116.38^{o}E, 39.98^{o}N, 92 m, urban	2008/06/22 -2009/04/16	CAPITAL INTERNATIONA	116.89^{o}E, 40.01^{o}N, 35.4 m
Wuxi	120.31^{o}E, 31.57^{o}N, 20 m, urban	2012/01/01 -2012/12/31	HONGQIAO INTL	121.34^{o}E, 31.20^{o}N, 3 m

1011

Table 2. Pixel-based evaluation of OMI NO$_2$ products with respect to MAX-DOAS for 162 pixels on 49 days.

	POMINO v1.1	POMINO	DOMINO v2	QA4ECV
Slope	0.95	0.78	1.06	0.66
Intercept (10^{15} molec. cm $^{-2}$)	-1.00	0.96	-3.86	1.09
R^2	0.80	0.80	0.68	0.75
NMB (%)	-3.4	-9.6	-2.1	-22.0

1012
1013

Table 3. Pixel-based evaluation of OMI NO_2 products with respect to MAX-DOAS for 27 pixels on 11 haze days [1].

	POMINO v1.1	POMINO	DOMINO v2	QA4ECV
Slope	1.07	0.80	1.11	0.58
Intercept (10^{15} molec. cm^{-2})	-3.58	1.76	-11.79	3.20
R^2	0.76	0.68	0.38	0.34
NMB (%)	4.4	-9.4	-5.0	-26.1

1014   1. The haze days are determined when the ground meteorological station data and
1015   MODIS/Aqua corrected reflectance (true color) data both indicate a haze day.
1016   Average across the pixels, AOD = 1.13 (median = 1.10), SSA = 0.90 (0.91), MAX-
1017   DOAS NO_2 = 51.92 x 10^{15} molec. cm^{-2}, and CF = 0.06 (0.03).

Table 4. Evaluation of OMI NO$_2$ products with respect to MAX-DOAS of 36 pixels on 18 cloud-free days[1].

	POMINO v1.1	POMINO	DOMINO v2	QA4ECV
Slope	1.30	1.13	0.92	0.79
Intercept (10^{15} molec. cm^{-2})	-0.61	0.31	2.32	1.05
R^2	0.55	0.56	0.53	0.63
NMB (%)	29.4	20.8	21.9	-5.8

1018   1. CF=0 in POMINO product. Average across the pixels, AOD = 0.60 (median = 0.47),

1019   SSA = 0.90 (0.91), and MAX-DOAS NO$_2$ = 26.82 x 10^{15} molec. cm^{-2}.
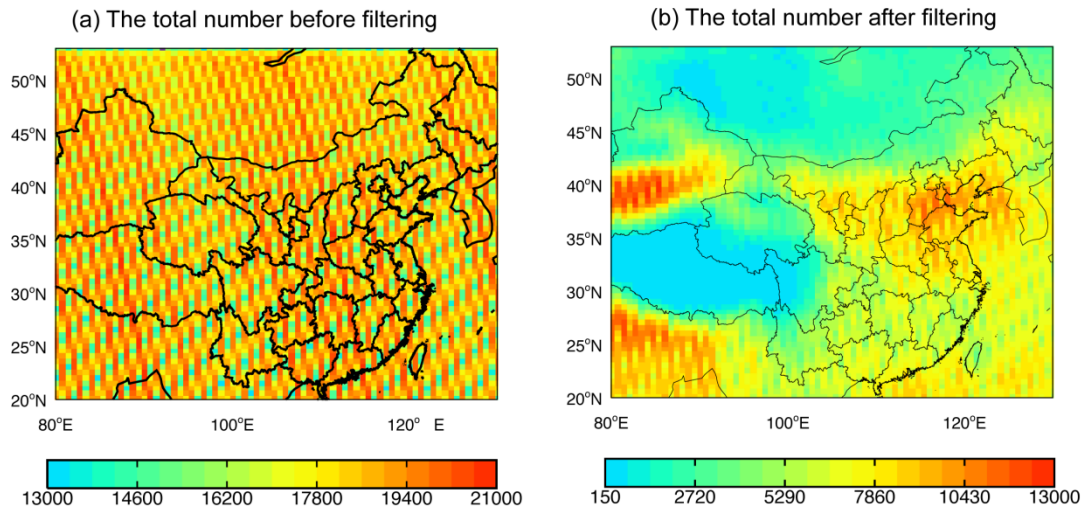
1020   Figure A1. The total number of CALIOP Level-2 aerosol extinction profiles at 532 nm

1021   used to derive our climatological (2007–2015) dataset on a 0.667^o long. x 0.5^o lat.

1022   grid (a) before and (b) after filtering.
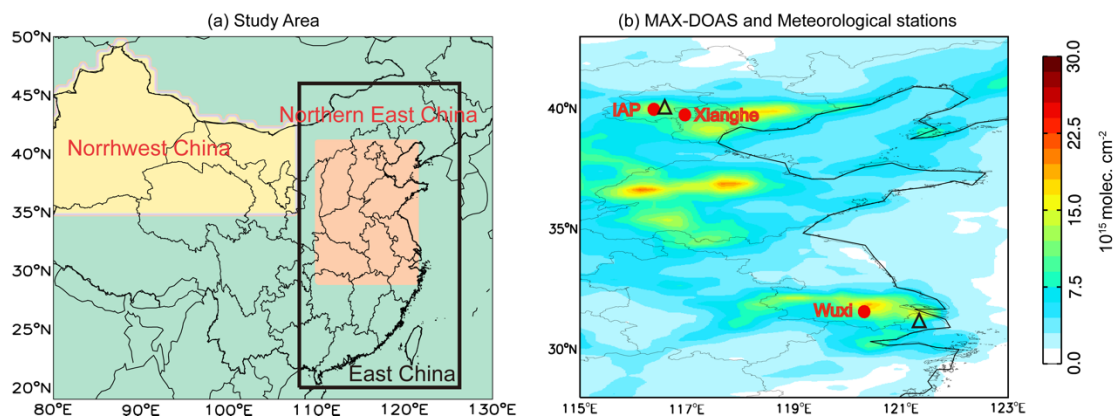
Figure 1. (a) Three study areas: Northern East China, Northwest China, and East China. (b) MAX-DOAS measurement sites (red dots) and corresponding meteorological stations (black triangle) overlaid on POMINO v1.1 NO$_2$ VCDs in August 2012.
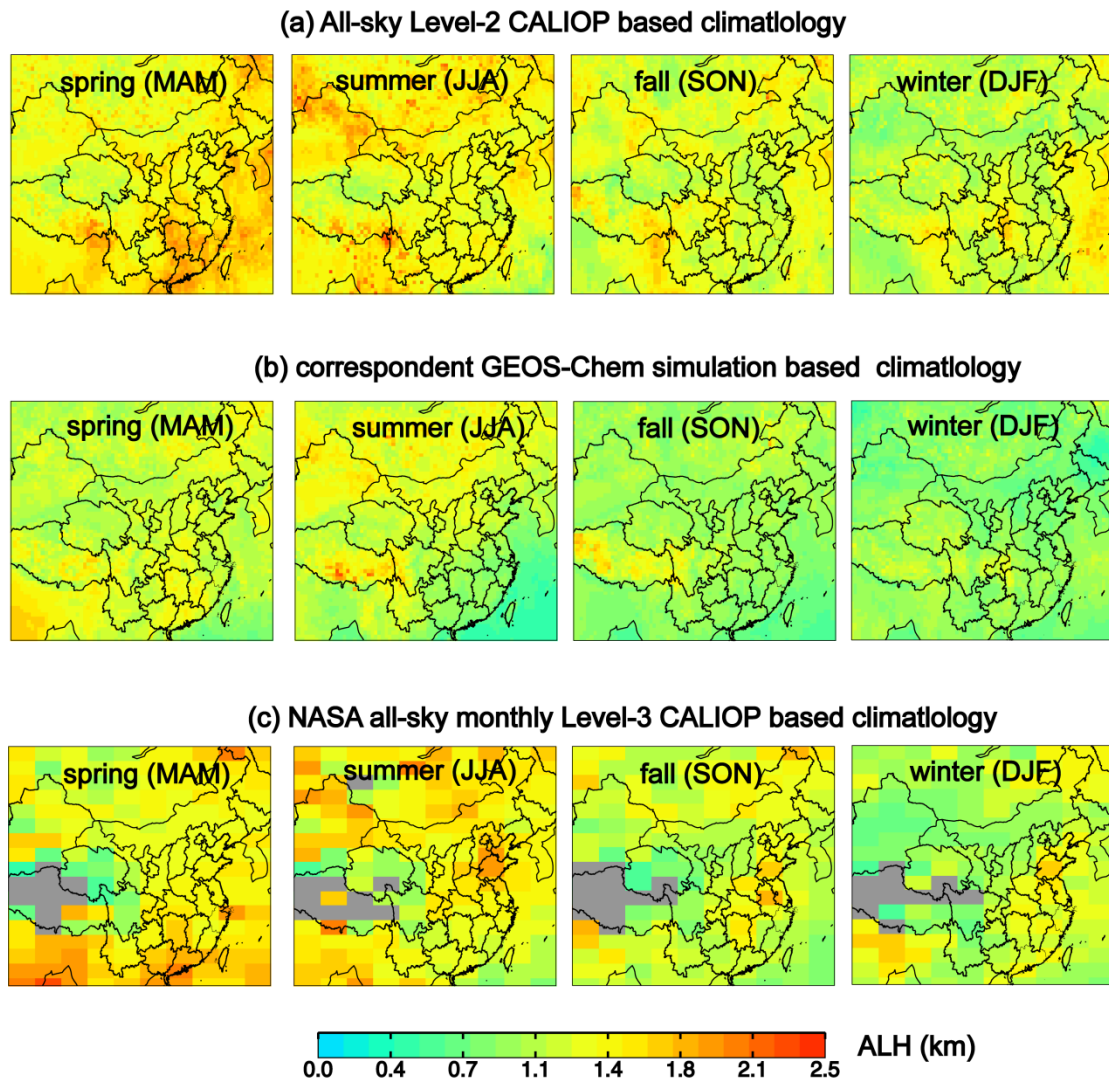
Figure 2. Seasonal spatial patterns of ALH climatology at 532 nm on a 0.667^0 long. x 0.50^0 lat. grid based on (a) our complied all-sky Level-2 CALIOP data, (b) corresponding GEOS-Chem simulations, and (c) NASA all-sky monthly Level-3 CALIOP dataset.
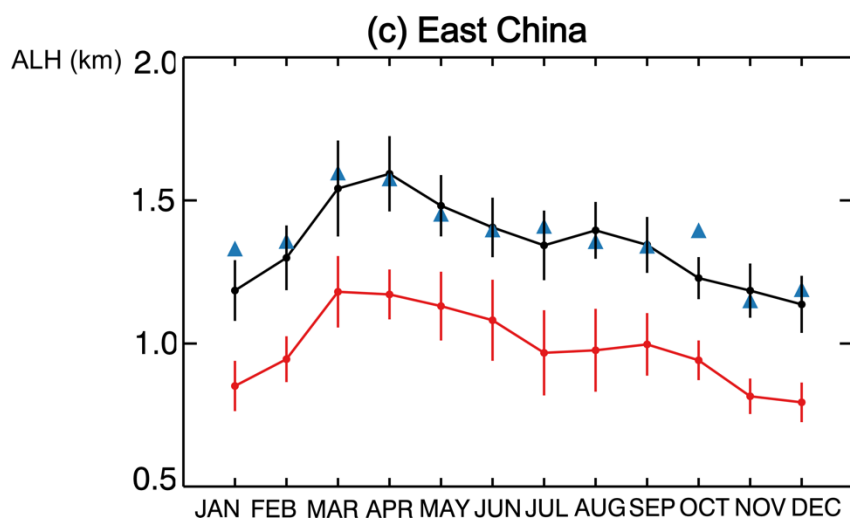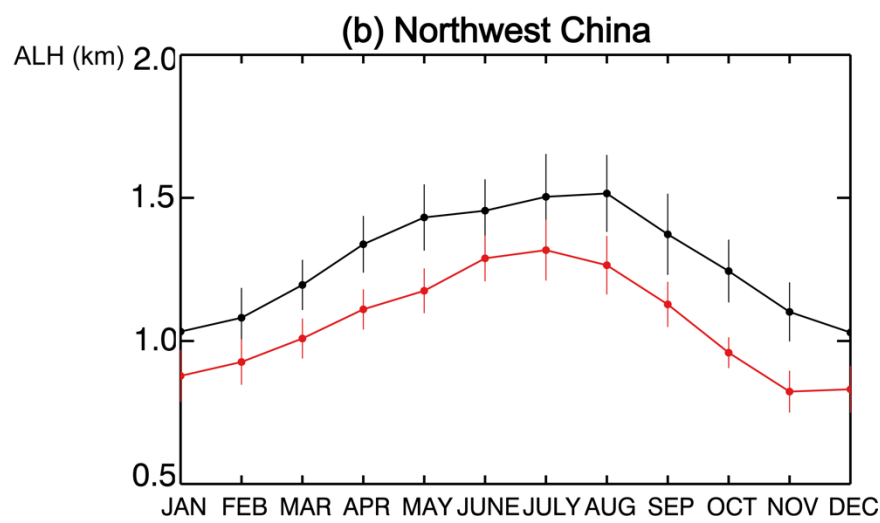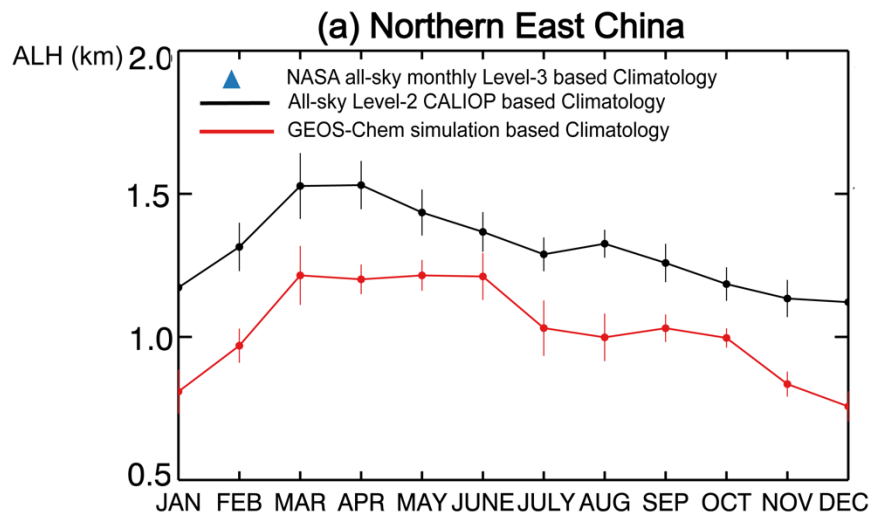
1030   Figure 3. Regional mean ALH monthly climatology over (a) Northern East China, (b)

1031   Northwest China, and (c) East China. The error bars stand for 1 standard deviation for

1032   spatial variability.

1033   50
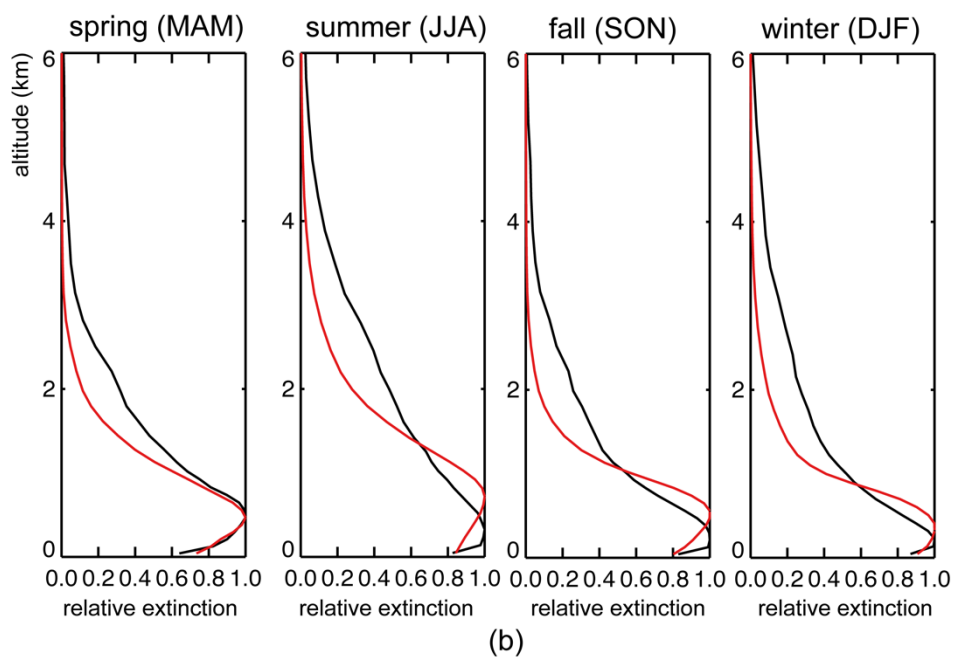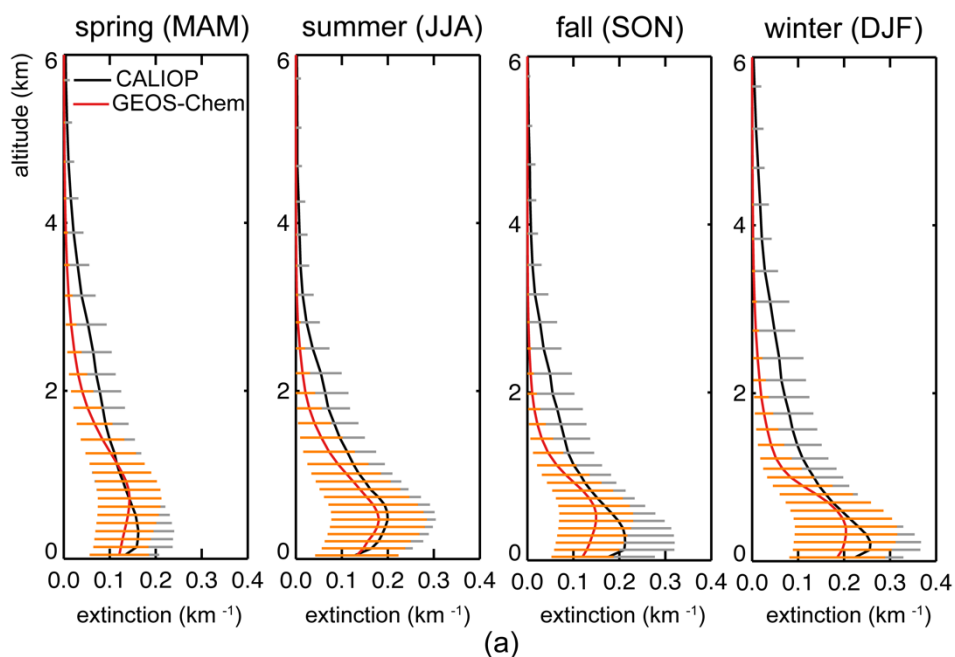
1034   Figure 4. Seasonal climatological aerosol extinction profiles (first row) and

1035   corresponding relative extinction profiles (normalized to maximum extinction values,

1036   second raw) in spring (MAM), summer (JJA), fall (SON) and winter (DJF) over

1037   Northern East China. Model results (in red) are prior to MODIS/Aqua based AOD

1038   adjustment. Error bars in (a) represent 1 standard deviation across all grid cells in each

1039   season.
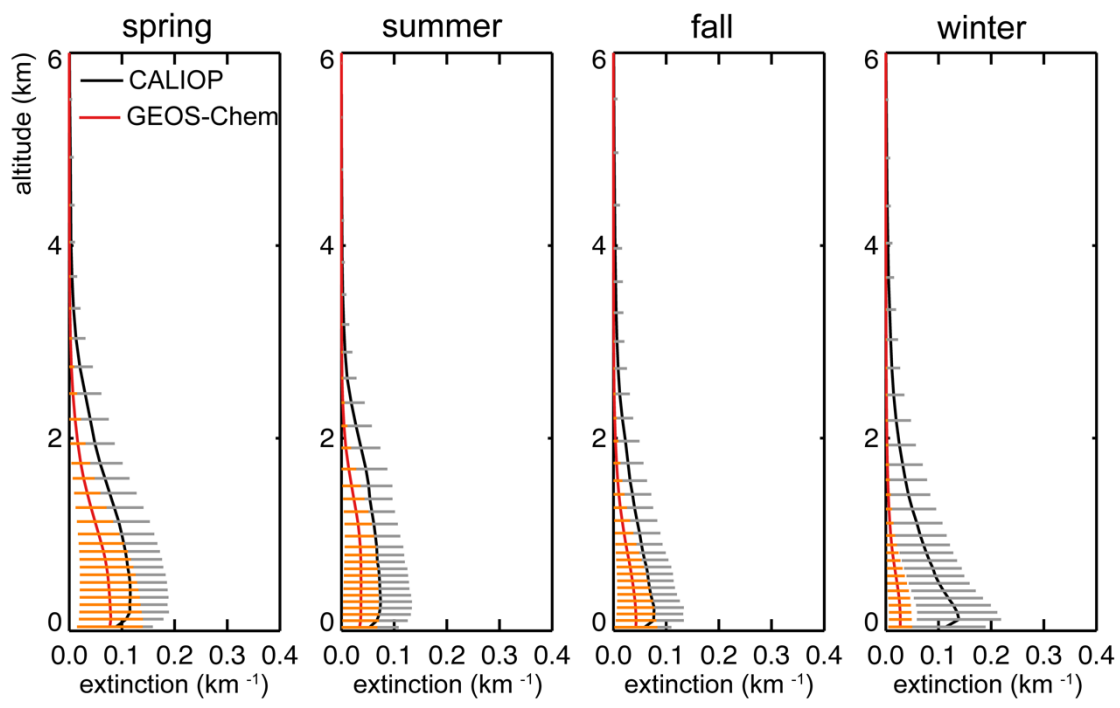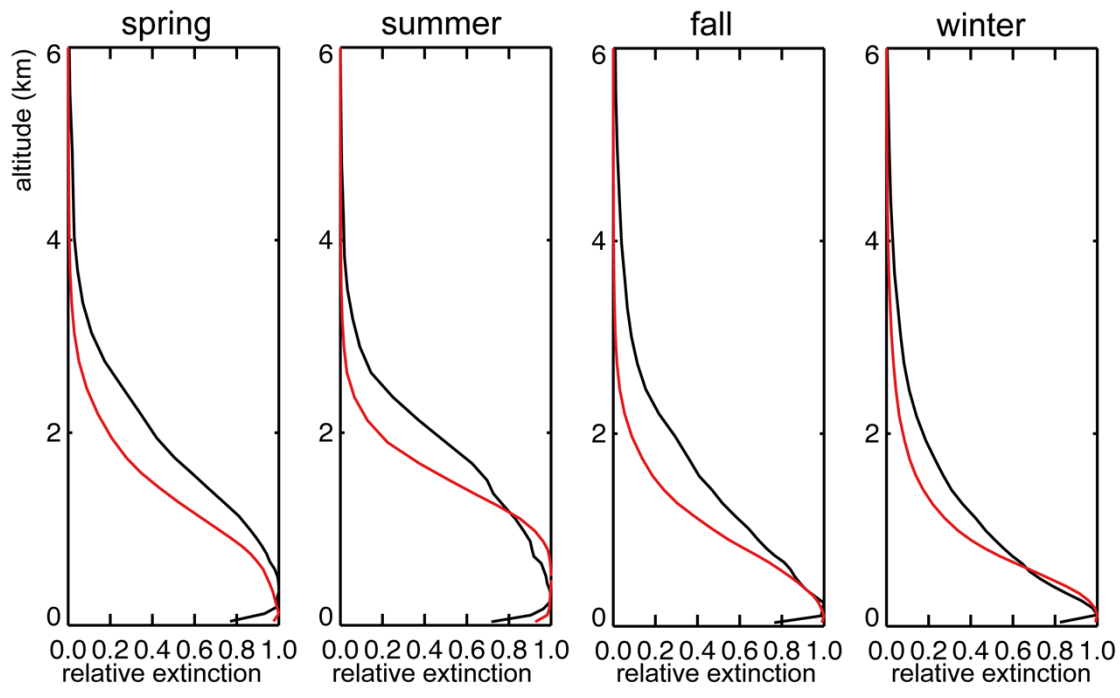
1040 Figure 5. Similar to Fig. 5 but for Northwest China.
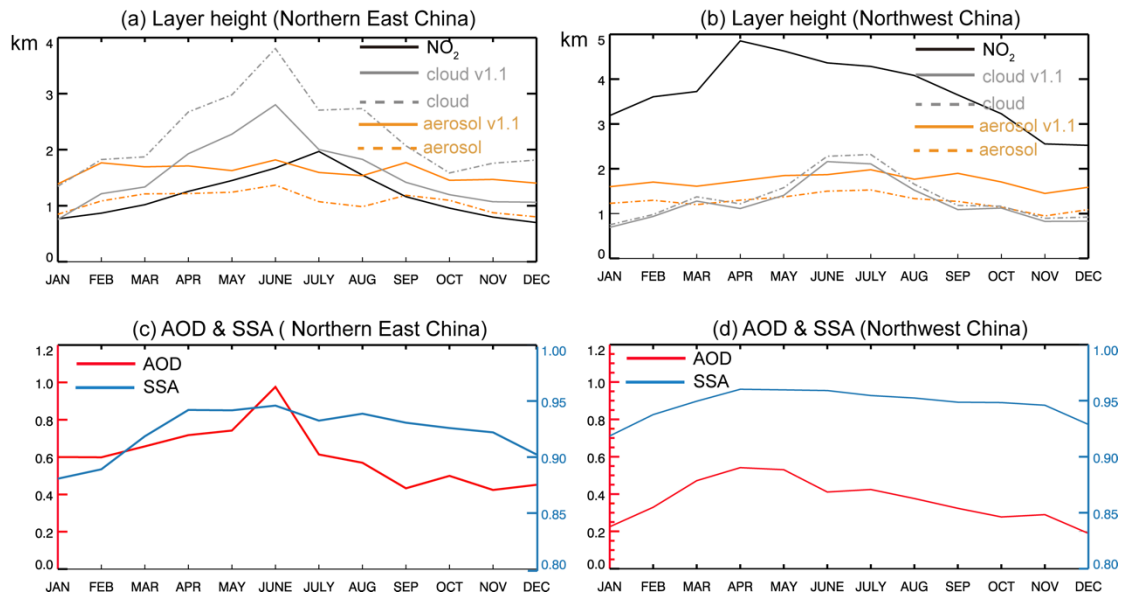
Figure 6. Monthly variations of ALH, CTH and NLH over (a) Northern East China and (b) Northwest China in 2012. Data are averaged across all pixels in each month and region. The grey and orange solid lines denote POMINO v1.1 results, while the corresponding dashed lines denote POMINO. (c–d) Corresponding monthly AOD and SSA.
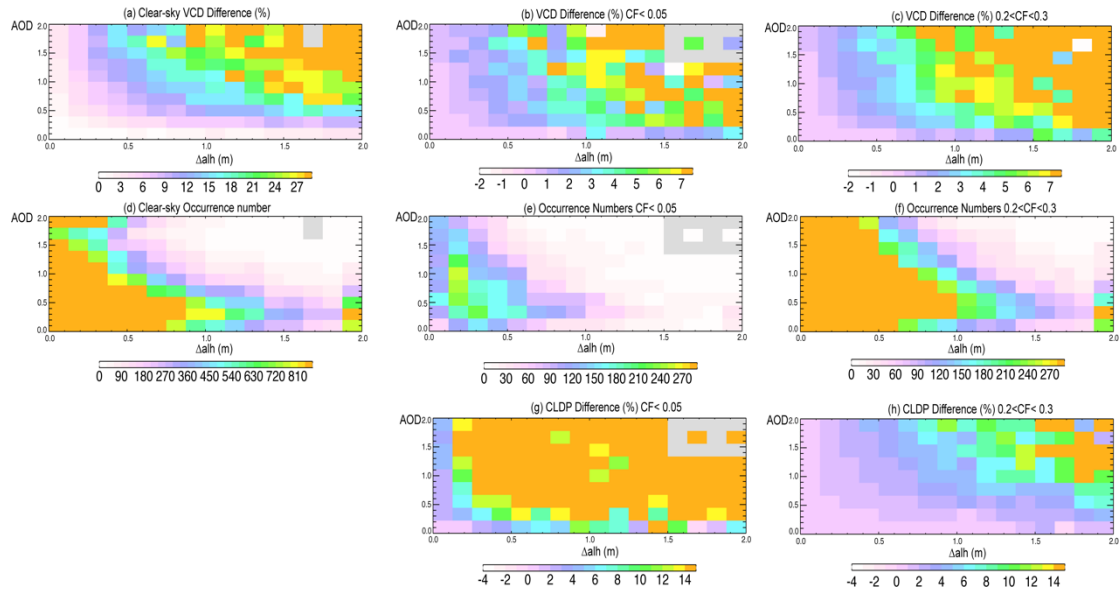
Figure 7. Percentage changes in VCD from POMINO to POMINO v1.1 ([POMINO v1.1 – POMINO] / POMINO) for each bin of ΔALH (bin size = 0.2 km) and AOD (bin size = 0.1) across pixels in 2012 over Northern East China, for (a) cloud-free sky (CF = 0 in POMINO), (b) little-cloudy sky, and (c) modestly cloudy sky. (d-f) The number of occurrences corresponding to (a-c). (g, h) Similar to (b, c) but for the percentage changes in cloud top pressure (CP).
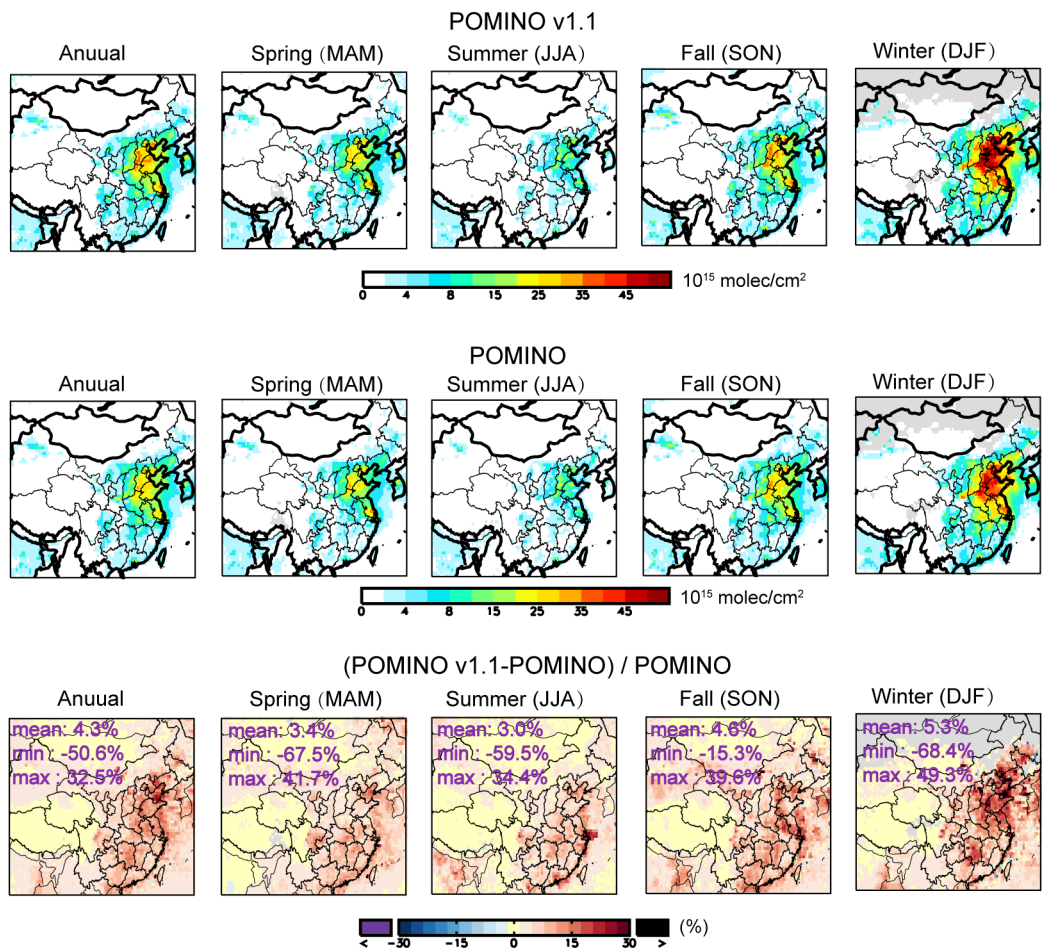
1052   Figure 8. Seasonal spatial distribution of tropospheric NO$_2$ VCD in 2012 for (a)

1053   POMINO v1.1, (b) POMINO, and (c) their relative difference.
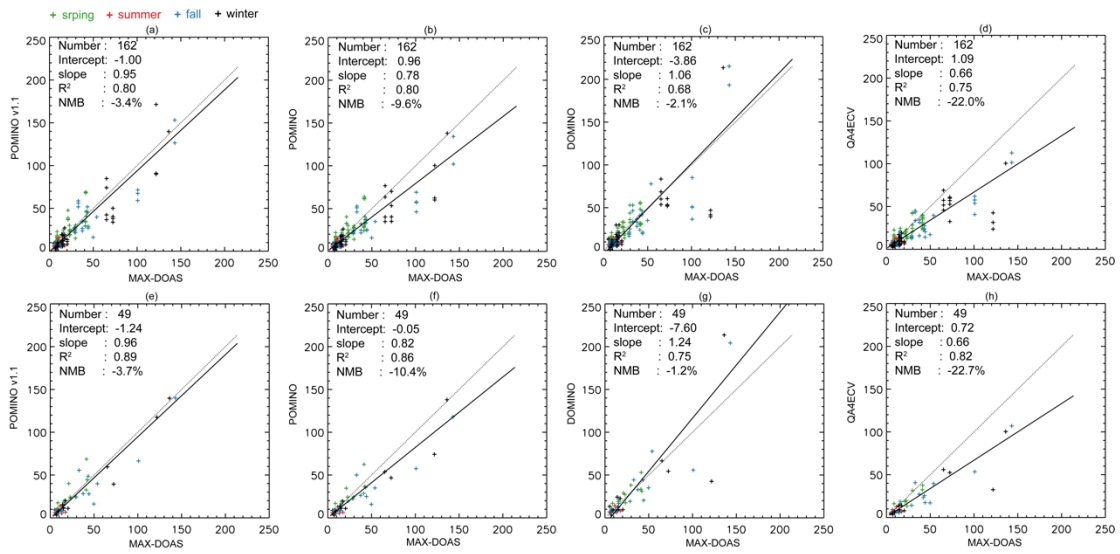
1054   Figure 9. (a–d) Scatterplot for NO$_2$ VCDs (10^{15} molec. cm^{-2}) between MAX-DOAS

1055   and each of the three OMI products. Each "+" corresponds to an OMI pixel, as several

1056   pixels may be available in a day. (e–h) Similar to (a–d) but after averaging over all OMI

1057   pixels in the same day, such that each "+" represents a day. Also shown are the statistic

1058   results from the RMA regression. The black solid line indicates the regression curve

1059   and the grey dotted line depict the 1:1 relationship.

1060

1061